

TRANSIENT DYNAMICS OF COMPOUND DROPS
IN SHEAR AND PRESSURE DRIVEN FLOW

A Dissertation
Submitted to the Faculty
of
Purdue University
by
Sangkyu Kim

In Partial Fulfillment of the
Requirements for the Degree
of
Doctor of Philosophy

December 2019
Purdue University
West Lafayette, Indiana

THE PURDUE UNIVERSITY GRADUATE SCHOOL
STATEMENT OF DISSERTATION APPROVAL

Dr. Sadegh Dabiri, Chair

School of Agricultural and Biological Engineering &
School of Mechanical Engineering

Dr. Osman Basaran

School of Chemical Engineering

Dr. Andrea Vacca

School of Mechanical Engineering &
School of Agricultural and Biological Engineering

Dr. Pavlos Vlachos

School of Mechanical Engineering

Approved by:

Dr. Nicole Key

Head of the Graduate Program

ACKNOWLEDGMENTS

Firstly, I would like to thank my advisor Dr. Sadegh Dabiri for his guidance and involvement in my Ph.D. studies. I sincerely appreciate his patience through my progress, contribution in carefully reviewing my writings, and guidance throughout my Ph.D. progress. I have been amazed and influenced by his passion for knowledge, professionalism, and intuition in fluid dynamics. He has given me the freedom to conduct research at my own pace in the direction of my choosing. When I had to reschedule my graduation plans due to a broken bone, he was very understanding and helpful throughout the process. I cannot thank him enough for all his contribution, guidance, time, and funding.

Besides my advisor, I would also like to thank my committee members, Dr. Pavlos Vlachos, Dr. Andrea Vacca, and Dr. Osman Basaran for kindly agreeing to be on my defense committee and for their time. Also, I want to thank all the professors and faculties at Purdue University for influencing the way I think, and for sharing their knowledge with their own perspectives. In particular, I want to thank Dr. Carlo Scalo, Dr. Arezoo Ardekani, Dr. Jun Chen, Dr. Steven Wereley, and Dr. Sam Midkiff for their impact on me as a researcher in computational fluid dynamics, and all the faculties in ME309 for providing me with a hands-on experience in fluid dynamics and in teaching.

I'd like to appreciate my fellow research colleagues, especially the students in our research group and Dr. Ardekani's research group, for sharing their ideas on many occasions. In particular, I would like to thank Pramod Bhuvankar for all the insightful discussions. I would also like to thank Pelin Bulutoğlu for all the help, especially the help getting through my clavicle fracture.

Lastly, I'd like to thank my family for their endless support. I wouldn't be here without the freedom and opportunity they provided me throughout my life as a student and now a researcher.

TABLE OF CONTENTS

	Page
LIST OF TABLES	vii
LIST OF FIGURES	viii
SYMBOLS	xiii
ABSTRACT	xv
1. INTRODUCTION	1
1.1 Dynamics of compound drops subject to a simple shear flow	4
1.2 Dynamics of compound drops subject to a Poiseuille flow	5
2. GOVERNING EQUATION AND NUMERICAL IMPLEMENTATION	7
2.1 Governing Equations	7
2.2 Characteristic Non-Dimensional Numbers	7
2.3 Numerical Implementation and Verification	9
3. DYNAMICS OF ECCENTRIC DOUBLE EMULSION DROPLETS IN A SIMPLE SHEAR FLOW	14
3.1 Problem Statement	14
3.2 Numerical Results and Discussion	15
3.2.1 Revolving and drifting of the inner droplet	15
3.2.2 Effect of radii ratio between inner and outer droplets	26
3.2.3 Effect of interfacial tension coefficient on migration	27
4. LATERAL MIGRATION DOUBLE EMULSION DROPLETS IN LOW REYNOLDS NUMBER POISEUILLE FLOW	32
4.1 Problem Statement	32
4.2 Results and Discussions	34
4.2.1 Equilibrium Configurations	34
4.2.2 Effect of Initial Placement on Stability	37
4.2.3 Effect of Geometric Parameters on the Equilibria	40
5. CROSS STREAM LIFT FORCE ON A COMPOUND DROP IN 3D RECT- ANGULAR POISEUILLE FLOW	44
5.1 Problem Statement	44
5.2 Results and Discussion	47
5.2.1 Effect of Radii Ratio on Lift Force	47
5.2.2 Effect of Outer Drop Viscosity on Lift Force	49
5.2.3 Discussion on Stable Compound Drop Control Design	51

	Page
5.2.4 Discussion on the Origin of the Lift Force	53
6. SUMMARY	61
REFERENCES	63
VITA	69

LIST OF TABLES

Table	Page
2.1 Grid convergence versus number of nodes across undeformed inner droplet diameter.	11
4.1 (a) Equilibrium configurations, (b) streamlines at channel midplane (xz or xy plane) in reference frame of outer drop with flow to the right, and (c) normalized flow direction averaged velocity profiles for (1) centerlined, (2) single vortex, (3) pair vortex (outer), and (4) pair vortex (inner) equilibria.	35

LIST OF FIGURES

Figure	Page
2.1 Grid independency test with 16, 32, and 64 grids across the initial inner droplet diameter. (a) inner drop Taylor deformation; (b) outer drop Taylor deformation; (c) normalized relative x -position of inner drop; (d) normalized relative y -position of inner drop. The local extrema are noted with circles in (c) and (d).	12
2.2 Outer drop deformation with $k = 0.5$ with varying Ca_o and $Ca_o = 0.025 - 0.25$. The deformation is averaged over time after a limit cycle behavior or steady state is reached, and compared against the compound drop results from Chen <i>et al.</i> [49] and simple drop results from Rumscheidt and Mason [68].	12
2.3 Eccentric compound droplet in 2D at steady state. For the 3 cases simulated, the inner droplet centers relative to the outer droplet are initially located at $(-1/4, 0)$, $(-\sqrt{2}/8, \sqrt{2}/8)$, and $(0, 1/4)$. The final compound droplet configurations agree with that from Hua <i>et al.</i> [50].	13
3.1 Schematic of the computational domain with a single undeformed double emulsion droplet with eccentricity in the y direction. The outer drop is positioned at the center of the domain, whereas the inner drop can be placed away from the center if an eccentricity is wanted. Boundaries at $y = \pm L_y/2$ are moving with an equal and opposite velocities $\pm \dot{\gamma} L_y/2$. The origin is set at the center of the computational domain. Schematic is not drawn to scale.	15
3.2 Inner droplet deformation, position, shape, and the velocity vectors tangent to the viewing plane. Taylor deformation, non-dimensional relative x , y , and z positions with initial eccentricity in the (a) x , (c) y , and (e) z -directions are shown; xy -plane view of the interfaces and the velocity vectors with eccentricity in the (b) x and (d) y -directions; (f) xz -plane view of the interfaces and the velocity vectors, magnified $\times 2$ for visibility, with eccentricity in the z -direction. The plane views (b), (d), and (f) are shown at times shaded in (a), (c) and (e).	17
3.3 Phase portraits of dimensionless relative (a) x -velocity and (b) y -velocity of the inner droplets versus the dimensionless relative position. The inner droplet is initially offset in the x -direction with magnitudes noted in the legend.	19

Figure	Page
3.4 The inertial effect on the revolving motion is investigated by increasing the shear rate with and without keeping Ca_o constant. Given an initial x -eccentricity, (a) D_i , (b) D_o , and (c) normalized distance from the inner drop center to the outer drop center, with local maxima noted with circles, are shown. The reversal in the outward motion with $Re = 5$ and $Ca_o = 0.2$ is due to a large deformation in the outer drop.	20
3.5 The streamlines inside the compound droplet at the mid-section with an initial x -eccentricity with (a) $Re = 5$ and $Ca_o = 0.05$ after reaching limit cycle behavior and (b) $Re = 5$ and $Ca_o = 0.2$ after reaching steady state. The larger deformation creates recirculation zones in (b), making a steady state obtainable.	21
3.6 (a) Phase portrait of dimensionless relative z -velocity versus position of the inner droplet. The inner drop is initially offset in the z -direction with the magnitudes indicated in the legend; (b) Dimensionless relative z -direction movement of the inner drop versus dimensionless time, given various initial offsets in the z -direction.	23
3.7 The inertial effect on the drifting motion is investigated by increasing the shear rate with and without keeping Ca_o constant. Given an initial z -eccentricity, (a) D_i , (b) D_o , and (c) normalized relative z -position of the inner drop are shown. The reversal in the drifting motion with $Re = 5$ and $Ca_o = 0.2$ is due to a large deformation in the outer drop, as was the case in the revolving motion.	23
3.8 Dimensionless (a) 3-D view of the migration path of the inner droplet initially placed at $(x, z) = (0.05, 0.05)$ with $k = 0.5$. The two black lines represent how the (b) xz -plane view and (c) yz -plane view are acquired when various initial eccentricities are tested. The initial positions are marked by triangles and the final by filled circles. The open diamonds denote the local maxima in (b) x and (c) y positions such that only the outward component of the motion is shown from the combination of revolving and drifting motions. The global maximum in x or y (<i>i.e.</i> envelope of the limit cycle) is shown with filled circles.	25
3.9 (a) xy -projection and (b) 3D view of the limit cycle movement of the center of the inner droplet with various initial (x, z) offsets noted in the legend. The normalized relative position of inner droplet is plotted for ~ 1.5 revolving cycle, and show a tilted elliptical pattern.	26

Figure	Page
3.10 Behavior of the inner droplet depending on the initial inner droplet placement and the radii ratio. Dimensionless (a) xz -plane view and (b) yz -plane view with the inner droplets initially placed with various (x, z) offsets with $k = 0.4$; dimensionless (c) xz -plane view and (d) yz -plane view with various (y, z) offsets with $k = 0.6$. Filled triangles, filled circles, and open diamonds are used in the manner similar to Fig. 3.8, and familiar outward migrations to when $k = 0.5$ are observed.	28
3.11 Dimensionless relative position of the inner droplet versus dimensionless time with various β . Normalized relative (a) x and (b) y positions are shown with dotted lines, with initial inner drop offset in the x -direction. The maxima in x and y positions are marked with circles and are connected; (c) normalized relative z -position is shown with initial inner drop offset in the z -direction.	29
3.12 The increase (filled upward triangle) and decrease (open downward triangle) of eccentricity in the Capillary number space with initial (a) x and (b) z eccentricity.	30
3.13 Comparison between $\beta = 0.1$ and $\beta = 0.2$ with initial (x, z) offsets of $(0.05, 0.05)$ and $(0.1, 0.1)$ with $Ca_o = 0.5$. Dimensionless (a) xz -plane view and (b) yz -plane views are shown in identical manner to Fig. 3.8 and Fig. 3.10. While the inner drop still moves away from the center of the outer droplet, the outward motion is no longer radial.	31
4.1 Schematic of the computational domain. A spherical and concentric compound drop is placed in a pressure driven channel. The channel initially has zero velocity and the flow is in the x -direction.	33
4.2 The effect of radii ratio and initial placements on the drop stability and migration paths are shown. Green circles denote initial placements that do not result in breakup and red circles denote initial placements that do. Black paths denote outer drop centroid movement and red inner. Migration paths associated with initial placements that result in breakup are not shown. The color contour shows the time of breakup. Only a portion of the channel is shown to scale to clearly show the migration paths.	38
4.3 Cases 1 through 4 denoted in Fig. 4.2 are more closely looked at. Distance between inner and outer drop centroids (blue), inner (red) and outer (black) drop deformations are shown on the left. Inner (red) and outer (black) drop movements in y and z direction are shown. Cases 3 and 4 are shown until breakup.	39

Figure	Page
4.4 The effect of size ratio of the compound drop to the channel and the radii ratio of the compound drop on the equilibrium position and the channel throughput.	41
4.5 Streamlines in the xy -plane view at the z -midplane with $\zeta = 0.8$. Pair vortex (outer) equilibrium is reached, but the significant wall effects position the compound drop at the center of the channel.	41
4.6 The effect of channel aspect ratio on the equilibrium positions of simple and compound drops, and on the channel throughput.	42
5.1 Schematic of the computational domain. A spherical and concentric compound drop is placed with symmetry about y , the short wall direction. Various compound drop placements along z , the long wall direction, is considered. The flow is initially parabolic, and is pressure driven in the x -direction.	45
5.2 The nondimensional lift force on a compound drop with various positions $z_o/L_z \leq 0.5$ with radii ratio $k = 0.6$. The Reynolds number is varied from 2.4 to 19.2.	48
5.3 The nondimensional lift force on simple and compound drops with various positions $z/L_z \leq 0.5$ and varying radii ratio $k = 0.4 - 0.6$. The hydraulic Reynolds number is 9.6. The filled in markers imply extrapolation as previously described.	49
5.4 The nondimensional lift force on simple drop and compound drop with various positions $z/L_z \leq 0.5$ and varying radii ratio $k = 0.4 - 0.6$. The hydraulic Reynolds number is 9.6. The simple drop viscosity and outer drop viscosities are varied as $\mu_{\text{new}}/\mu_{\text{old}} = [1/2, 1, 2]$. The filled in markers imply extrapolation.	50
5.5 (Left): The nondimensional minimum distance between inner and outer interfaces with varying Ca_o with $k = 0.6$ and (right): the corresponding lift force profile.	52
5.6 The nondimensional simple drop or outer drop Taylor deformation of a simple drop or compound drops with varying radii ratio. The filled markers imply extrapolated deformation.	54
5.7 The nondimensional Taylor deformation of a simple drop and compound drops with varying radii ratio. The viscosities of simple drop or outer drop are varied as $\mu_{\text{new}}/\mu_{\text{old}} = [1/2, 1, 2]$. The filled markers imply extrapolated deformation.	55
5.8 The nondimensional slip velocity, effective shear rate, and rotation rate of the simple and compound drops.	56

Figure	Page
5.9 Magnus force and Saffman lift force, calculated based on Fig. 5.8	57
5.10 Lift force difference between simple drop and compound drops. The simple drop lift force is taken as baseline and the difference to compound drop lift is shown, based on (left): the measurement (Fig. 5.3) and (right): The Magnus and Saffman forces combined (Fig. 5.9.)	59
5.11 The non-dimensional slip velocity over simple and compound drops with varying radii ratio and varying viscosities. The viscosities of simple drop or outer drop are varied as $\mu_{\text{new}}/\mu_{\text{old}} = [1/2, 1, 2]$	60

SYMBOLS

ρ^I	density of background fluid
ρ^{II}	density of outer drop fluid
ρ^{III}	density of inner drop fluid
\mathbf{u}	velocity field
p	pressure field
μ^I	viscosity of background fluid
μ^{II}	viscosity of outer drop fluid
μ^{III}	viscosity of inner drop fluid
\mathbf{D}	strain rate tensor
σ_i	interfacial tension coefficient at the inner interface
σ_o	interfacial tension coefficient at the outer interface
κ_i	curvature of the inner interface
κ_o	curvature of the outer interface
R_i	radius of undeformed inner drop
R_o	radius of undeformed outer drop
Re	Reynolds number
Ca	Capillary number
k	ratio of the inner to outer radius
β	ratio of the inner to outer interfacial tension coefficient
\mathbf{I}	second moment of inertia
D_i	Taylor deformation number of inner interface
D_o	Taylor deformation number of outer interface
L_x	length of computational domain in x direction
L_y	length of computational domain in y direction
L_z	length of computational domain in z direction

t	time
$\dot{\gamma}, G$	shear rate
ϵ	aspect ratio of rectangular channel
ζ	ratio of outer drop diameter to channel width
γ_P, γ_I	PID controller constants
D_H, H	hydraulic diameter of channel
U_c	channel average velocity
U	channel maximum velocity
a	spherical particle diameter
u_f	background fluid velocity
u_p	particle velocity

ABSTRACT

Kim, Sangkyu PhD, Purdue University, December 2019. Transient Dynamics of Compound Drops in Shear and Pressure Driven Flow . Major Professor: Sadegh Dabiri, School of Mechanical Engineering.

Multiphase flows abound in nature and enterprises. Our daily interactions with fluids - washing, drinking, and cooking, for example - occur at a free surface and within the realm of multiphase flows. The applications of multiphase flows within the context of emulsions, which are caused by mixing two immiscible fluids, have been of interest since the nineteenth century: compartmentalizing one fluid in another is particularly of interest in applications in pharmaceutical, materials, microfluidics, chemical, and biological engineering. Even more control in compartmentalization and delivery can be obtained through the usage of double emulsions, which are emulsions of smaller drops (*i.e.*, inner drop) within larger drops (*i.e.*, outer drop). The goal of this work is to understand the dynamic behavior of compound drops in confined flow at low Reynolds numbers. These behaviors include the migration patterns, limit cycles, and equilibrium locations in confined flows such as channel flows.

Firstly, we look at non-concentric compound drops that are subject to simple shear flows. The eccentricity in the inner drop is either within the plane of shear, normal to the plane of shear, or mixed. We show unreported motions that persist throughout time regardless of the initial eccentricity, given that the deformations of the inner and outer drops are small. Understanding the temporal dynamics of compound drops within the simple shear flow, one of the simplest background flows that may be imposed, allows us to probe at the dynamics of more complicated background flows.

Secondly, we look at the lateral migration of compound drops in a Poiseuille flow. Depending on the initial condition, we show that there are multiple equilibria. We also show that the majority of initial configurations results in the compound drop

with symmetry about the short wall direction. We then show the time it takes for the interfaces to merge if a given initial configuration does not reach the aforementioned symmetry.

Thirdly, while the different equilibria of compound drops offer some positional differences at different radii ratio, we show that the lift force profiles at non-equilibrium locations offer distinctly different results for compound drops with different radii ratio. We then look at how this effect is greater than changes that arise due to viscosity ratio changes, and offer insights on what may create such a change in the lift force profile.

1. INTRODUCTION

Multiphase flow, a simultaneous flow of materials with different phases or materials with same phase but different chemical properties, abounds in nature and the enterprises. The day-to-day interactions with liquids in ordinary households, ranging from the dripping of a faucet, drinking of water, to washing and cooking, are almost always at a free surface. The distinguishing feature of such flows is, unlike a confined flow where the enclosing boundary dictates the flow domain, the presence of free boundaries separate at least two phases. Within the realm of multiphase flows, the study of free surface flows has been of considerable interest for both scientific and industrial purposes.

Mixing two immiscible fluids can produce emulsions, which is a dispersion of droplets of one fluid within the second. Emulsions (or drops) are often not in total equilibrium, but are often metastable, and the integrity of the non-trivial boundaries are retained for extended amount of time especially in the presence of surfactants, which can stabilize the liquid-to-liquid interface. Emulsions play crucial roles in many chemical engineering applications such as in coatings, food, pharmaceuticals, and cosmetics [1]. The fundamental scientific and industrial interest in compartmentalizing one fluid in another goes back as far as the early nineteenth century [2, 3]. Compared to a simple drop, where one liquid is emulsified within another, even more flexibility and control in encapsulation of fluid can be obtained through the usage of double emulsion droplets.

A double emulsion droplet, also called a compound droplet or simply a double emulsion, is a nested liquid droplet system of three immiscible fluids. In this thesis, the inner-most fluid will be called the inner drop, the nesting fluid the outer drop, and the background carrier of the compound drops the surrounding fluid. Typically, the fluids composition that describes a double emulsions are water-in-oil-in-water or oil-in-

water-in-water, but recently all-aqueous double emulsions have also been reported [4]. Because the inner-most fluid is not making contact with the surrounding fluid, the usage of compound droplets as a predictable chemical delivery system has a significant impact in many fields including pharmaceutical [5], materials [6], microfluidics [7], and biological engineering [8]. Furthermore, compound droplets can be used to model cells [9] and may also occur naturally in the ocean [10]. As such, researchers have focused on the stable production methods, steady state configurations in various surrounding flows, stability associated with migration processes, and reliable breaking (release) mechanisms of compound droplets [11–13].

Typically, compound drops are produced in a two-step process, where the inner drop is first emulsified into the fluid that eventually forms the outer drop, and then through a second emulsification step [14]. Controlling the dispersity at each emulsification step is important, since polydispersity of the final compound drop is compounded by error at each emulsification stage. As such, microfluidics [15] or flow with co-axial flows [16] as a means of ensuring the uniformity of compound drops are preferred, and so the Reynolds number of interest regarding compound drops is usually low.

While Chambers and Kopac were the first to report the liquid-liquid compound drops [17, 18], Torza and Mason [19] were the first to thoroughly investigate the interactions of three different phases and found various steady state configurations in the absence of gravity. Their method of analysis focused on the energy considerations based on the interfacial tension coefficients, and considered fully-engulfed droplets (meaning the inner drop does not make contact with the surrounding fluid) as well as partially engulfed compound droplets.

When fluid motions are considered, the related viscous effects greatly alter and complicate the compound drop configurations. This complexity has heavily impacted the analytical progress, but attempts have been made to analytically solve for the flow inside and around a compound droplet; using Lamb’s solution technique in spherical geometry [20], Taylor [21] predicted the deformation of a simple droplet under a simple shear. Following Taylor’s work, Cox [22] the deformation of a concentric

compound droplet under a time-dependent flow. Following a similar formulation, Stone and Leal [23] solved for the velocity and pressure field inside and around a concentric and spherical compound droplet, then solved for the first order deformation by matching the normal stress of spherical droplet to an interfacial tension stress due to a small deformation. They then verified and expanded upon the analytical work using the boundary integral method. Following the work from Stone and Leal, Qu and Wang [24] used spectral boundary element method to verify the predicted deformation in extensional flows, and investigated the effects of inner droplet placement; the inner drop was eccentrically placed in the plane of the surrounding extensional shear flow such that the geometry was symmetric in the direction normal to that plane.

Because Lamb’s solution is limited to spherical geometry, Sadhal and Oguz [25] utilized a bipolar coordinate system to solve for the Stokes flow of an eccentric compound droplet in a uniform flow. This eccentric solution was further investigated by Song, Xu, and Yang [26], who solved for the compound droplet in a cylindrical Poiseuille flow. In the last two studies, the compound droplet and the incoming flow were confined to an axisymmetric geometry, and the eccentricity of the inner droplet was parallel to the imposed surrounding flow. Analyses performed by Stone and Leal, Qu and Wang, and Sadhal and Oguz have been extended by Mandal, Ghosh, and Chakraborty [27], who included the effect of surfactant. They also solved for the migration of an eccentric compound drop under an axisymmetric flow using bipolar coordinate system, and found that the eccentricity increases when the initial eccentricity is above a critical value. Additionally, the Lorentz reciprocal theorem was used by Haj-Hariri, Nadim, and Borhan to solve for the concentric compound drops in a general Stokes flow [28].

While the migration of solid spheres or single-phase droplets and deformation dynamics of single-phase droplets due to the surrounding flows are well known [29–43], the same cannot be said for compound droplets. Moreover, the literature on compound droplets is heavily centered towards production schemes and steady state behaviors, and is scarce on temporal response. Although the steady state configurations of various

droplets within given channels are vital in utilizing flow-focusing techniques and in controlling the break-up of droplets [44], the temporal evolutions and the feedback effects of droplets are equally important in many ways: first, as demonstrated for the case of simple droplets [45], in predicting the velocity and pressure feedback effects from already-produced droplets, which enables a stable compound droplet production mechanism; second, in understanding and predicting when and how the break-up of compound droplets may occur [46]; and third, in characterizing the stability of a given configuration of double emulsions [25].

1.1 Dynamics of compound drops subject to a simple shear flow

Chen *et al.* [47–49] tested the extensional characteristics and breakup mechanisms when a single compound droplet is subjected to a shear flow by using both numerical and experimental tools. They found different steady-state regimes and breakup mechanisms for varying capillary numbers, radii ratio, and shear conditions. Interestingly, they found that the inner drop does not always suppress the deformation of the outer drop. Hua *et al.* [50] found similar steady-state deformations in 2D and 3D simulations with concentrically placed compound droplets. They also reported, through 2D numerical investigations, that eccentrically placed inner droplets in various positions all transitioned to the same concentric steady configuration under simple shear.

Patlazhan *et al.* [51] also looked at two-dimensional compound droplets under shear flow by considering wall-confinement effects, and found non-monotonic deformation as a function of the radii ratio and non-monotonic steady-state orientation as a function of channel narrowing. By varying the Capillary number and the ratio of the interfacial tension coefficients, Smith, Ottino, and Olvera de la Cruz found multiple break-up patterns when a compound drop is subjected to shear flow and then is allowed to relax [52].

Currently, to the best of our knowledge, there is no literature on the temporal dynamics of eccentric compound droplets that have no symmetry relative to the

geometry of the imposed background flow. It is well known that simple drops and compound drops can breakup in a shear flow [29, 47, 48], and also that the dynamics in shear flows can offer invaluable insight in understanding the dynamics in other flows [53]. In this light, the first step in understanding the temporal dynamics of double emulsion droplets is in studying the response of eccentric compound drops in a simple shear flow. The response of compound droplets to other more complicated flows can be better understood by decomposing the imposed flows into a simple shear flow and other fundamental flows. With this in mind, we present the temporal dynamics of compound drops subject to a simple shear flow in chapter 3, where we emphasize the temporal evolution of deformation and inner drop's position relative to the outer drop.

1.2 Dynamics of compound drops subject to a Poiseuille flow

The lateral migration of rigid spheres in Poiseuille flow is well-understood. In Stokes flow, a rigid spherical particle does not show lateral migration [33]. When inertial effects are present, spherical particles in a cylindrical Poiseuille flow migrate to an annulus at roughly 0.6 radius of the pipe [34, 35, 54]. This annulus is known as the Segrè-Silberberg annulus. Recently, an inward accumulation of particles at an inner annulus has been observed at $Re > 600$ [55]. This annulus has been termed inner Segrè-Silberberg annulus, and its emergence is numerically shown to be suppressed by additional hydrodynamics with periodic cells [56].

When the channel cross section is square or rectangular, spherical particles migrate to eight equilibrium positions - four next to the midpoint at each wall, and four next to the corners, where the preferred position is dependent upon the Reynolds number [36–39].

On the other hand, simple drops show a different cross stream migration than spherical particles do due to the presence of deformation and the internal fluid circulation. In axisymmetric Poiseuille flow with low Reynolds number, simple drops with a moderate viscosity ratio to the surrounding fluid migrate towards the tube

center [40–42]. In a 3D Poiseuille flow in a rectangular channel with an aspect ratio of 2, simple drops migrate to two equilibrium positions found at a given Reynolds number, and the equilibrium position moves closer to the centerline with an increase in the Reynolds number due to the larger deformation [43]. Additionally, Raffiee *et al.* [57] showed that deformable cells in Newtonian and polymeric fluids migrate to the focal position along the channel diagonal.

The literature on the migration dynamics of compound drops subject to Poiseuille flow is scarce. Researchers have used bipolar coordinate system to analytically solve for the migration when the deformation is small [26, 27], or computational methods to simulate large deformations [58, 59]. However, to the authors’ knowledge, no cross-stream migration of compound drops has been investigated thus far. Bearing this in mind, we consider the lateral migration of compound drops in a three-dimensional rectangular channel in chapter 4. The flow within the channel is pressure driven with a low Reynolds number of $Re = O(1)$. We mainly look at a compound drop whose size is comparable to the channel size, and background velocity field that is imposed onto the compound drop does not closely resemble a simple shear flow. Therefore, we focus on the migration of compound drops into multiple equilibria given various initial conditions.

2. GOVERNING EQUATION AND NUMERICAL IMPLEMENTATION

2.1 Governing Equations

We consider a compound droplet that is subject to an arbitrary background flow. The different and immiscible fluid phases are incompressible and Newtonian with densities ρ^Φ and viscosities μ^Φ , where Φ ranges from I to III. We let phase I denote the surrounding fluid, II the outer droplet, and III the inner droplet. We define the interface between phases I and II as the outer interface, and that between II and III as the inner interface. We also define the interfacial tension coefficients, σ_i and σ_o , for the inner and outer interfaces. The governing equations for the unsteady and incompressible viscous flows are given by the Navier-Stokes equations,

$$\rho^\Phi \left(\frac{\partial \mathbf{u}}{\partial t} + \mathbf{u} \cdot \nabla \mathbf{u} \right) = -\nabla p + \nabla \cdot (2\mu^\Phi \mathbf{D}) + \int_i \sigma_i \kappa_i \delta(d_i) \mathbf{n}_i dA_i + \int_o \sigma_o \kappa_o \delta(d_o) \mathbf{n}_o dA_o, \quad \nabla \cdot \mathbf{u} = 0, \quad (2.1)$$

where \mathbf{u} is the velocity vector, p is the pressure, $\mathbf{D} = \frac{1}{2}[\nabla \mathbf{u} + (\nabla \mathbf{u})^T]$ is the strain rate tensor, κ_i and κ_o are the curvatures associated with the inner and outer interfaces, δ is the Dirac delta function, d_i and d_o are the distances from the respective interfaces, \mathbf{n}_i and \mathbf{n}_o are the unit normal vectors at the interfaces, and dA_i and dA_o are the area element at the interfaces. The effect of gravity is not considered.

2.2 Characteristic Non-Dimensional Numbers

Let R_i and R_o be the initially undeformed and spherical radii of the inner and outer droplets, then we can characterize the flow with the following non-dimensional parameters:

$$\text{Reynolds number: } Re = \frac{\rho^I U R_o}{\mu^I} \quad (2.2)$$

$$\text{Capillary numbers: } Ca_i = \frac{\mu^I U}{\sigma_i}, \quad Ca_o = \frac{\mu^I U}{\sigma_o} \quad (2.3)$$

$$\text{Radii ratio: } k = \frac{R_i}{R_o} \quad (2.4)$$

$$\text{Interfacial tension coefficient ratio: } \beta = \frac{\sigma_i}{\sigma_o}. \quad (2.5)$$

The characteristic velocity U depends on the type of flow at hand. When we consider a compound drop in a simple shear flow, it is given in terms of the multiple of the imposed background shear rate $\dot{\gamma}$ and the relevant length scale, which is R_i for the inner drop and R_o for the outer drop. Therefore,

$$\text{Reynolds number: } Re = \frac{\rho^I \dot{\gamma} R_o^2}{\mu^I} \quad (2.6)$$

$$\text{Capillary numbers: } Ca_i = \frac{\mu^I \dot{\gamma} R_i}{\sigma_i}, \quad Ca_o = \frac{\mu^I \dot{\gamma} R_o}{\sigma_o} \quad (2.7)$$

On the other hand, when we consider a compound drop in a pressure-driven flow, the characteristic velocity is given in terms of the channel average velocity in the flow direction, U_c . Unlike the shear driven case, it is common to use the diameter as the characteristic length for calculating the Reynolds number in a pressure driven flow. Thus,

$$\text{Reynolds number: } Re = \frac{\rho^I U_c (2R_o)}{\mu^I} \quad (2.8)$$

$$\text{Capillary numbers: } Ca_i = \frac{\mu^I U_c}{\sigma_i}, \quad Ca_o = \frac{\mu^I U_c}{\sigma_o} \quad (2.9)$$

In this work, we look at $Re = O(1)$, $k = 0.4 - 0.6$, $Ca = O(0.01) - O(0.1)$, and $\beta = 0.1 - 1$. Due to the low Reynolds number that is typically associated with double emulsions, the ratio of the densities does not play an important role.

Additionally, we quantify the deformation of both the inner and outer droplets by using

$$\chi = \sqrt{I_{\max}/I_{\min}}, \quad (2.10)$$

the square root of the ratio of the largest and smallest eigenvalues of the second moment of inertia tensor, which in turn is quantified as [60]

$$I_{lm} = \frac{1}{\text{Vol}} \int_{\text{droplet}} (x_l - x_{lc})(x_m - x_{mc}) dV. \quad (2.11)$$

Here, Vol is the volume of a given droplet (whether it be inner or outer), x_l and x_m are the general coordinates, and x_{lc} and x_{mc} are the droplet's centroids in the l and m directions. The deformation χ has been shown to correspond to the aspect ratio of a droplet for a small deformation [61], and can be cast into Taylor deformation number [62] for the inner and outer interfaces as

$$D_i = \frac{L_i - B_i}{L_i + B_i} = \frac{\chi_i - 1}{\chi_i + 1}, \quad D_o = \frac{L_o - B_o}{L_o + B_o} = \frac{\chi_o - 1}{\chi_o + 1}, \quad (2.12)$$

where L and B are the instantaneous major and minor axes of the respective interfaces.

2.3 Numerical Implementation and Verification

We use finite-volume method on a three-dimensional staggered grid to discretize and solve for the numerical solution of the unsteady Navier-Stokes equations. We compute the advective terms using the Quadratic Upstream Interpolation for Convective Kinematics (QUICK) scheme [63] and solve for the pressure-velocity coupling using the projection method [64], which is numerically implemented using the Hypre library [65]. We represent the interfaces with unstructured grids using front-tracking method [66]; the interfaces of the inner and outer drops are not allowed to make topological changes (*e.g.* break-up or merge). This corresponds to the physical case of a dilute surfactant concentration that prevents the merging of the surfaces [67], yet does not affect the interfacial tension. Finally, we advance the solution in time with 2nd order explicit Euler method using Courant-Friedrichs-Lewy condition of 0.9.

First we perform a grid refinement test. We consider the case of a simple-shear driven compound droplet. The exact problem statement and the geometry are shown in Fig. 3.1 in Chapter 3. The length scale is non-dimensionalized by the diameter of the undeformed outer droplet, and the time-scale by the shear rate of the imposed

background simple shear. A single compound droplet, initially undeformed with $R_o = 0.5$ and $R_i = 0.25$, is placed in the center of a shear-driven domain of size $L_x \times L_y \times L_z = 2 \times 2 \times 2$ with a shear rate of $\dot{\gamma} = 1$. The uniform viscosities and densities are chosen such that $Re = 1.25$, and the interfacial tension coefficients are chosen such that $Ca_i = 0.025$ and $Ca_o = 0.05$. The inner drop's center is offset from that of the outer drop in the x -direction by $R_o/4$. The domain is uniformly divided into 64^3 , 128^3 , and 256^3 grids, giving 16, 32, and 64 grids across the initially undeformed inner droplet diameter.

The comparison of Taylor deformation and inner droplet position relative to the outer droplet are shown in Fig. 2.1, where the local extrema in relative position are circled. The positions of the inner and outer droplets, $\mathbf{x}_i = (x_i, y_i, z_i)$ and $\mathbf{x}_o = (x_o, y_o, z_o)$, are computed by taking the center of mass of the respective phases, and the relative position is then acquired as $\mathbf{x}_i - \mathbf{x}_o$. We find a good agreement in the relative position of the inner droplet with 16, 32, or 64 grids across the inner drop diameter, and in the deformations with 32 or 64. The first local extrema are tabulated in Table 2.1 alongside a comparison of the relative position at the time when the first extremum occurs with coarse grid.

We notice an abrupt change in D_i for $\dot{\gamma}t < 1$, similarly noted by Chen *et al.* [48]. This initial jump seems to not have been caused by a specific treatment of the initial computational domain, as simulations with initially quiescent domain as well as simple shear profile domain both show this behavior. Rather, it seems to arise from the deformation of the outer droplet, and the resulting flow field inside. The outer drop's deformation in steady state or limit cycle behavior (which will be later described) matches well with Chen *et al.* [49] with 32 grids across the inner diameter, as shown in Fig. 2.2; a slight difference with $Ca_o = 0.1$ likely arises because the stable configuration in our simulations was an eccentric compound drop, whereas Chen *et al.* looked at the deformation of a concentric compound droplet. The deformation with Ca_o matches better because the stable configuration in our simulations was a concentric configuration. The transition from eccentric to concentric configuration

Table 2.1. : Grid convergence versus number of nodes across undeformed inner droplet diameter.

	Coarse (16)	Medium (32)	Fine (64)
First $(x_i - x_o)/2R_o$ extrema	-0.1440	-0.1441	-0.1438
$(x_i - x_o)/2R_o$ @ $t = 6.88$	-0.1440	-0.1441	-0.1438
First $(y_i - y_o)/2R_o$ extrema	-0.2242	-0.2233	-0.2284
$(y_i - y_o)/2R_o$ @ $t = 4.85$	-0.2242	-0.2232	-0.2228

will be described later. Simple drop deformation from Rumscheidt and Mason [68] is also shown for comparison.

The difference due to grid spacing in the relative positions of the inner droplet is less than 1%, as shown in Table 2.1. On the other hand, the deformation data shows a close convergence between medium and fine grids. We therefore use 32 grid points across the inner droplet for all remaining numerical calculations when we look at the dynamics of compound drops subject to simple shear flow. Also for convenience, we refer to the center of mass of the inner and outer droplets as simply their positions. Because the positions of the droplets can vary depending on the starting configurations, we look at the relative position of the inner droplet to the outer droplet.

On the other hand, the parameter space that we cover when we look at the dynamics of compound drops subject to Poiseuille flow is much larger, and so we use uniform grid with 16 grid points across the undeformed inner droplet diameter. While the sweeping of parameter space is mainly performed at this coarser grid resolution, to ensure that numerical simulations are accurate, we verify the existence of four distinct equilibria configurations by having 32 grid points across the undeformed inner droplet diameter.

We also verify the validity of the code against the results from Hua *et al.* [50]. For this, the code is modified for 2D simulations, and cases 1, 2, and 3 outlined in section 4.2.3 of Hua *et al.* are tested; here, $Re = 1$ and $Ca_o = 0.25$ with $k = 0.5$. The inner

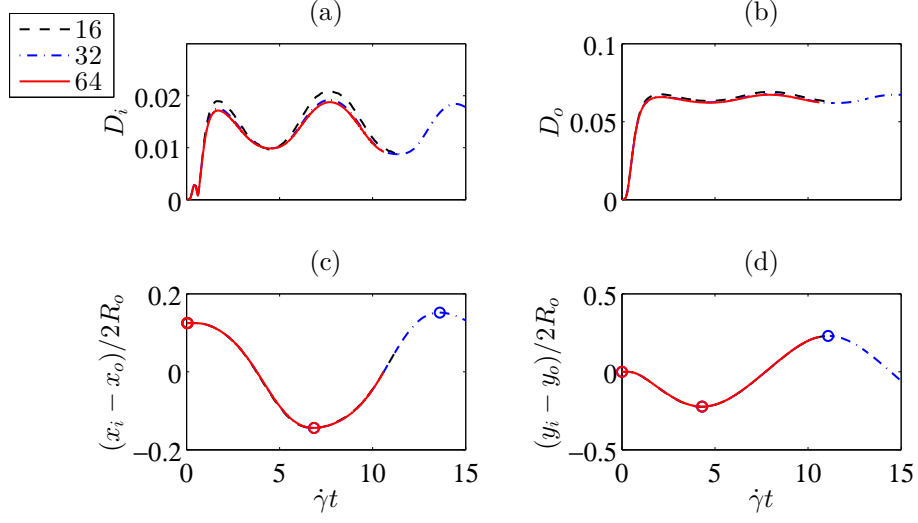


Figure 2.1. : Grid independency test with 16, 32, and 64 grids across the initial inner droplet diameter. (a) inner drop Taylor deformation; (b) outer drop Taylor deformation; (c) normalized relative x -position of inner drop; (d) normalized relative y -position of inner drop. The local extrema are noted with circles in (c) and (d).

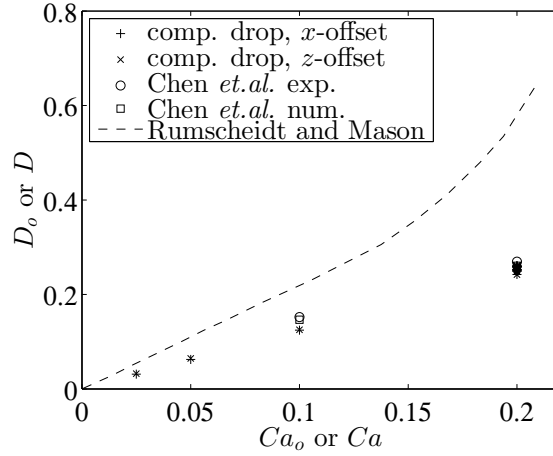


Figure 2.2. : Outer drop deformation with $k = 0.5$ with varying Ca_o and $Ca_o = 0.025 - 0.25$. The deformation is averaged over time after a limit cycle behavior or steady state is reached, and compared against the compound drop results from Chen *et al.* [49] and simple drop results from Rumscheidt and Mason [68].

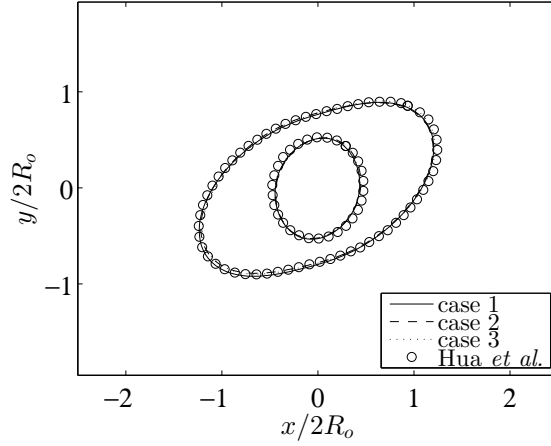


Figure 2.3. : Eccentric compound droplet in 2D at steady state. For the 3 cases simulated, the inner droplet centers relative to the outer droplet are initially located at $(-1/4, 0)$, $(-\sqrt{2}/8, \sqrt{2}/8)$, and $(0, 1/4)$. The final compound droplet configurations agree with that from Hua *et al.* [50].

droplet center is initially located at $(-1/4, 0)$, $(-\sqrt{2}/8, \sqrt{2}/8)$, and $(0, 1/4)$ relative to the outer droplet. As shown in Fig. 2.3, the interfaces at steady state show a good qualitative match with the results presented by Hua *et al.*.

3. DYNAMICS OF ECCENTRIC DOUBLE EMULSION DROPLETS IN A SIMPLE SHEAR FLOW

The main objectives of this chapter are threefold: first, to constitute the two fundamental motions - “revolving” and “drifting” - observed for an eccentric compound droplet exposed to a simple shear flow; second, to show how the two motions can be combined to collapse the motion of the inner droplet into a limit cycle; and third, to discuss the effects of the initial eccentricity, radii ratio, and the interfacial tension coefficients. In short, we demonstrate that the eccentricity of an inner droplet is always accentuated when all the fluids have the same viscosities and when the deformations are small, meaning that the inner droplet always moves towards the outer interface until only a thin film remains between the inner and outer interfaces. We also briefly discuss the mechanism by which the increase in eccentricity may be suppressed.

3.1 Problem Statement

We consider a compound droplet that is suspended in a shear flow as shown in Fig. 3.1. With the origin defined at the center of the computational domain, the background shear is defined by $\mathbf{u}_\infty = \dot{\gamma}y\hat{i}$ and is imposed by the velocity boundary condition at the top and bottom walls (*i.e.* walls normal to the y -direction) that are driven in the $\pm x$ -direction with equal and opposite velocities $\pm\dot{\gamma}L_y/2$. The other boundaries are periodic.

The compound droplet is initially undeformed with $R_o = 0.5$ and $R_i = 0.25$. The domain is of size $L_x \times L_y \times L_z = 2 \times 2 \times 2$ with a shear rate of $\dot{\gamma} = 1$. The uniform viscosities and densities are such that $Re = 1.25$, and the interfacial tension coefficients are such that $Ca_i = 0.025$ and $Ca_o = 0.05$.

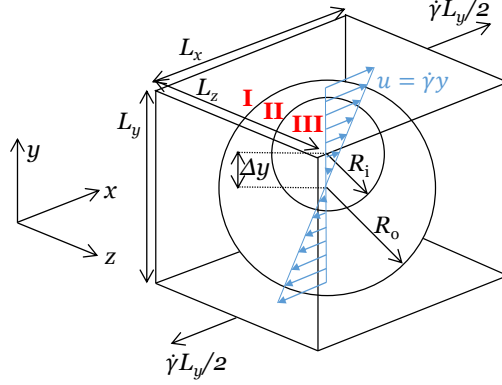


Figure 3.1. : Schematic of the computational domain with a single undeformed double emulsion droplet with eccentricity in the y direction. The outer drop is positioned at the center of the domain, whereas the inner drop can be placed away from the center if an eccentricity is wanted. Boundaries at $y = \pm L_y/2$ are moving with an equal and opposite velocities $\pm \dot{\gamma} L_y/2$. The origin is set at the center of the computational domain. Schematic is not drawn to scale.

In this chapter, we do not look into its effect of having different viscosities between different phases. As previously mentioned, the inertial effects are minimal since the Reynolds number of interest are small, and so all phases are have equal densities. Therefore, all the three phases are chosen to have uniform densities and viscosities.

3.2 Numerical Results and Discussion

3.2.1 Revolving and drifting of the inner droplet

We examine the effect of eccentricity by initially displacing the inner droplet in the x , y , and z directions by $R_i/2$. The Taylor deformation number and the relative position between the inner and outer droplets, $x_i - x_o$, $y_i - y_o$, and $z_i - z_o$, are shown in Fig. 3.2a, 3.2c, and 3.2e after non-dimensionalization. The relative positions whose magnitude variations are on the order of 10^{-4} , which is an order of magnitude smaller than the grid spacing, are not shown. The absolute position of the outer drop, which

will be representative of the position of the compound drop as a whole, is not shown because the overall movement in the x and z directions is not meaningful due to the nature of the periodic domain and because there is no movement in the y direction.

The droplet positions, shapes, and the tangential velocity field at the mid-section of the outer droplets are shown in Fig. 3.2b, 3.2d, and 3.2f. The viewing planes are chosen to show the direction of the significant inner droplet movement, and the velocity magnitudes are multiplied twofold in Fig. 3.2f for visibility.

Two very distinct motions are readily observed: one where the inner droplet persists in a “revolving” motion in the xy -plane (plane of shear) with almost no change in its z -position (the direction normal to the plane of shear), and the other where there is no revolving motion, but only a “drifting” motion in the z -direction. The characteristics of “revolving” and “drifting” motions are further explained in the following subsections.

Revolving motion in the plane of shear

We observe a persistent circulatory movement of the inner droplet when it is eccentrically placed with x or y offset. Fig. 3.2a, 3.2b, 3.2c, and 3.2d illustrate that the inner droplet migrates outward while orbiting about the center of the outer drop until a limit cycle behavior is reached; during the limit cycle, the inner drop continues to revolve about the center of the outer drop, but is no longer able to move outward because the interfaces almost touch; the interfaces do not actually come into contact, and a thin liquid film forms for portions of the limit cycle. The trajectory of the inner drop in limit cycle resembles a slanted ellipse, and is described in more detail in Section 3.2.1. Due to both the elongation of the outer droplet and also the slanted elliptical limit cycle, the inner droplet almost touches the outer droplet’s interface for only parts of a revolving cycle; *e.g.* the two interfaces are not very close to each other at $\dot{\gamma}t = 86.98$ but are at $\dot{\gamma}t = 90.64$ in Fig. 3.2d. This causes the outer drop’s deformation

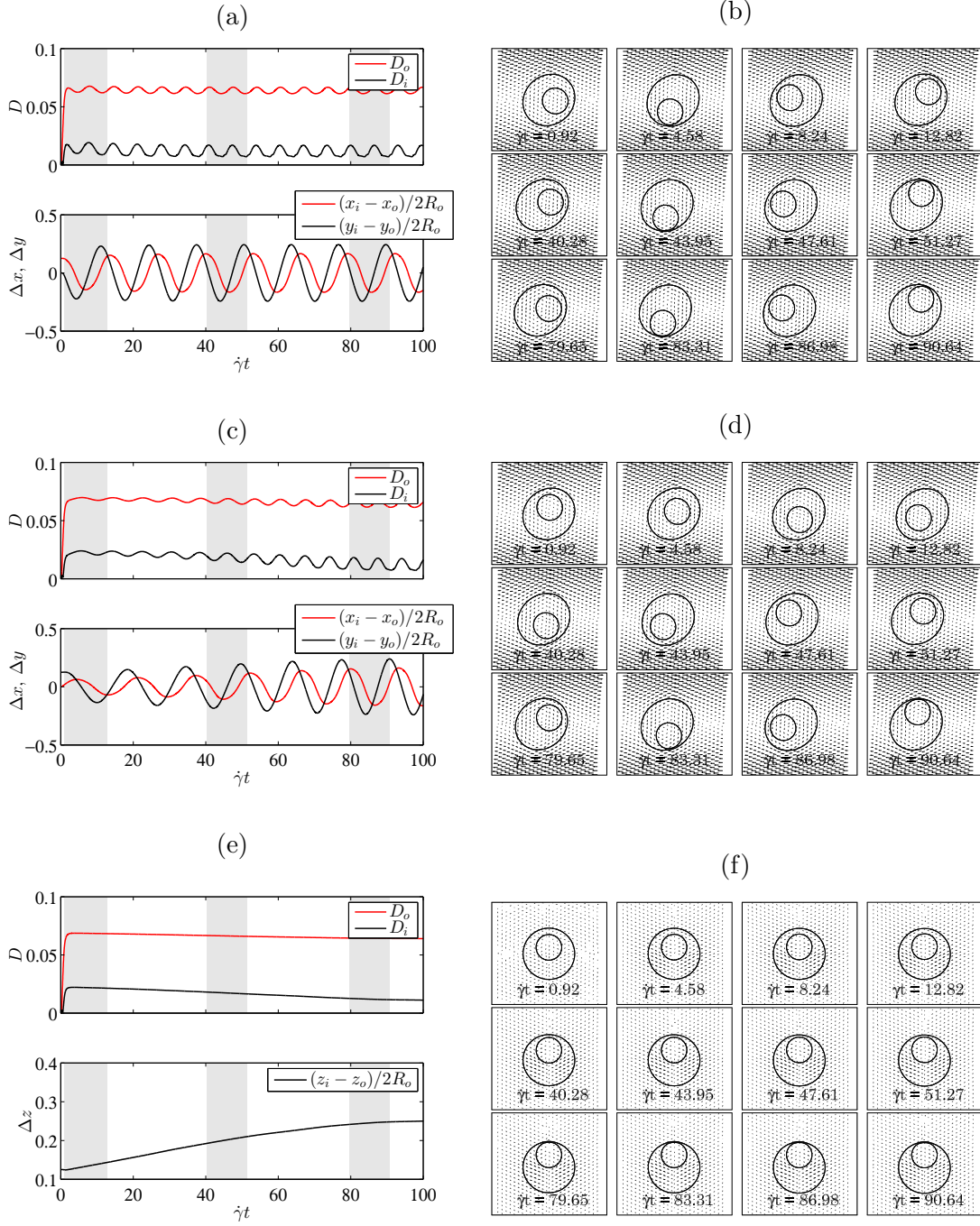


Figure 3.2. : Inner droplet deformation, position, shape, and the velocity vectors tangent to the viewing plane. Taylor deformation, non-dimensional relative x , y , and z positions with initial eccentricity in the (a) x , (c) y , and (e) z -directions are shown; xy -plane view of the interfaces and the velocity vectors with eccentricity in the (b) x and (d) y -directions; (f) xz -plane view of the interfaces and the velocity vectors, magnified $\times 2$ for visibility, with eccentricity in the z -direction. The plane views (b), (d), and (f) are shown at times shaded in (a), (c) and (e).

to undergo “breathing,” fluctuating at twice the frequency of the oscillation in the x and y positions.

The fact that the y -eccentricity case reaches limit cycle behavior when $\dot{\gamma}t \sim 100$ is not clear in Fig. 3.2c, but can be realized from Fig. 3.2d since the interfaces are almost touching when $\dot{\gamma}t \sim 90.64$, implying no more outward motion. In fact, all cases were run until $\dot{\gamma}t = 200$ to ensure that the limit cycle has been reached, but only the range $\dot{\gamma}t = [0, 100]$ is shown in Fig. 3.2. At first glance, it seems that the x -eccentricity case reaches limit cycle more quickly than the y -eccentricity case. This is reflective of the initial condition rather than the qualitative characteristic of the revolving motion: since the movement of the inner drop in the x and y directions is coupled by the revolving motion, different initial x and y eccentricities serve as different initial conditions to the fundamentally identical outward orbiting motion. Fig. 3.2b and 3.2d further show that having an initial x or y eccentricity in the inner droplet placement does not affect the final limit cycle, and Fig. Fig. 3.2a and 3.2c show the offset positions and the Taylor deformations match well after limit cycles are reached.

Simulating multiple offsets in the x -direction reveals that the revolving motion is ubiquitous and alike despite the varying degree of offsets, and that the revolving motions starting with different initial eccentricity all collapse to the same limit cycle. This fact is illustrated in Fig. 3.3 by phase portraits of inner droplet’s velocity versus position.

Based on the flow field inside a simple drop subject to a shear flow, a similar revolving motion of the inner droplet was assumed by Klahn *et al.* [46] in characterizing the escape mechanism of an inner droplet. However, their assumption was that a given inner droplet is bound to the concentrically elliptical streamlines that it was originally placed in, and therefore coalescence between multiple inner droplets was suggested as a means of escaping such a confinement. On the contrary, the results given here demonstrate that inner droplets are capable of moving radially outward without coalescence, so long as an initial offset in the plane of shear is realized. Chen

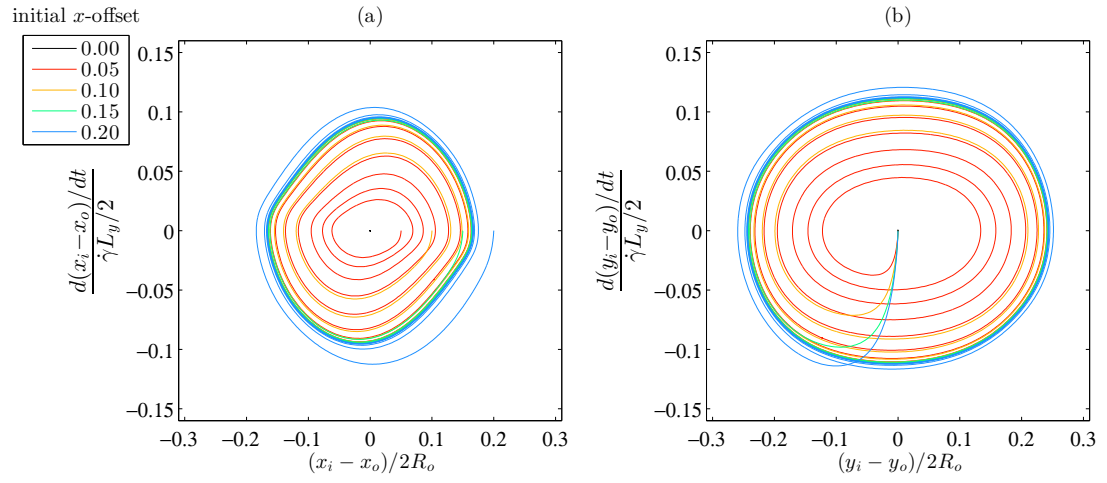


Figure 3.3. : Phase portraits of dimensionless relative (a) x -velocity and (b) y -velocity of the inner droplets versus the dimensionless relative position. The inner droplet is initially offset in the x -direction with magnitudes noted in the legend.

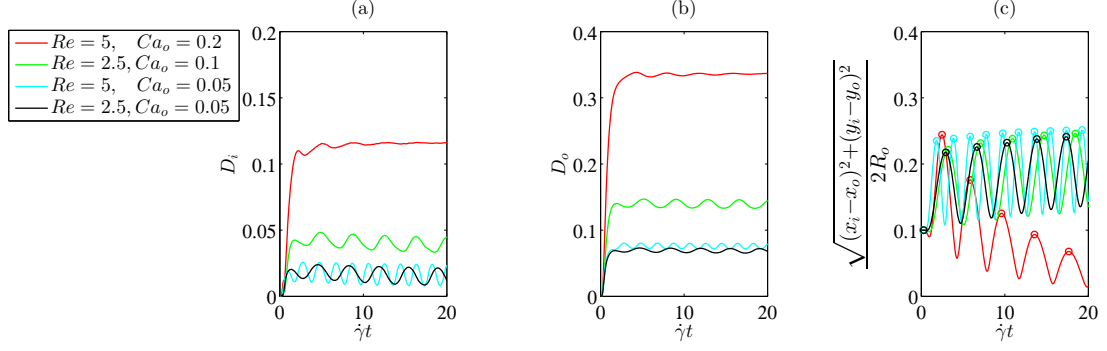


Figure 3.4. : The inertial effect on the revolving motion is investigated by increasing the shear rate with and without keeping Ca_o constant. Given an initial x -eccentricity, (a) D_i , (b) D_o , and (c) normalized distance from the inner drop center to the outer drop center, with local maxima noted with circles, are shown. The reversal in the outward motion with $Re = 5$ and $Ca_o = 0.2$ is due to a large deformation in the outer drop.

et al. also reported a circulatory streamline inside the outer droplet, but did not observe a revolving motion. We believe this is due to the much smaller Reynolds number they had ($Re \sim 10^{-5}$), which would have retarded the amplitude increase of the eccentricity from the nearly concentric compound droplets they had.

The outward motion is driven by the pressure force and the shear stress, and is not affected by the inertial effects as long as the deformations are small. The lack of inertial impact on the outward motion can be seen by increasing the shear rate, as can be seen in Fig. 3.4. Even after increasing the Reynolds number by a factor of 4, the outward motion is preserved so long as deformations are controlled by simultaneously increasing the inner and outer interfaces' tension coefficients to keep Ca_o and Ca_i constant.

We do see a reversal in the outward motion when $Re = 5$ and $Ca_o = 0.2$. This is not an inertial effect, but rather a deformation effect. This fact is well illustrated in Fig. 3.5: when the deformation of the outer drop is sufficient, recirculation zones are created inside the outer drop, creating a stable configuration. This transition of

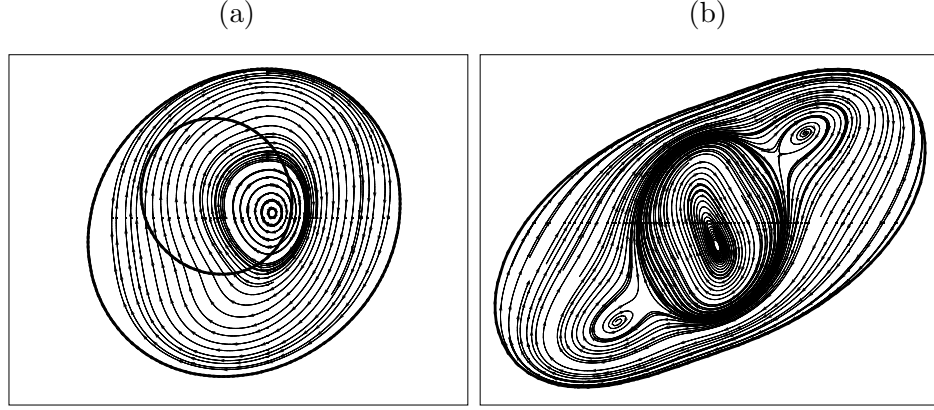


Figure 3.5. : The streamlines inside the compound droplet at the mid-section with an initial x -eccentricity with (a) $Re = 5$ and $Ca_o = 0.05$ after reaching limit cycle behavior and (b) $Re = 5$ and $Ca_o = 0.2$ after reaching steady state. The larger deformation creates recirculation zones in (b), making a steady state obtainable.

streamlines is similar to what was observed for a compound vesicle (a simple drop with a membrane and with a particle inner core) by Veerapaneni *et al.* when it underwent the transition from tank-treading to tumbling [69]. The fact that the creation of recirculation zones within the outer drop contributes to a transition in dynamics was also found by Zhou *et al.* who saw a non-monotonic relationship between k and the time a compound drop takes to squeeze through a choke in a pressure-driven flow [58].

The critical Capillary number for the transition from reaching limit cycle to reaching steady state lies between $0.1 < Ca_o < 0.2$, given that $Ca_i = 0.15$. The critical transition Ca_o depends on the deformation of the inner drop, *i.e.* on Ca_i and possibly k . Generally speaking, $D_o > D_i$, so there is little room left for examining the effect of increase in Ca_o past $Ca_o = 0.2$ before break-up occurs. The effect of Ca_o and Ca_i are discussed in more detail in Section 3.2.3. The effect of k on the transition Ca_o is not quantified in this work, but its presence can be deduced from the fact that k affects the outer drop deformation [49] and creation of recirculation zones [58, 69].

Drifting motion normal to the plane of shear

Unlike the pure revolving motion, the motion in the xy -plane is negligible when the inner droplet is initially displaced in only the z -direction. Rather, the inner droplet slowly drifts in the direction of the offset (which is the direction normal to the plane of shear), increasing in eccentricity until only a thin liquid film remains between the interfaces (see Fig. 3.2e and 3.2f). Such a movement is, to the authors' knowledge, unprecedented. The previous literature with eccentric compound droplets were either confined to having the eccentricity along the flow direction or within the plane of the surrounding flow [24–27].

Having various offsets in the z -direction all results in the same behavior, and the inner droplet always moves in the direction that increases the offset. Moreover, the drift velocities for different offset distances collapse into a single curve as shown in Fig. 3.6a, where the initial z -offsets are noted in the legend; the initial spikes are due to the computational domain being initially quiescent. The fact that all velocities collapse independently of the offset magnitude indicates that the drifting motion is a fundamental behavior of compound droplets in a shear flow; surprisingly, this collapse holds even for eccentricities that are on the order of the droplet radii. The time variation of the drifting motion with varying initial eccentricity is explicitly shown in Fig. 3.6b.

As was the case with revolving motion, the drifting motion does not seem to be caused by inertial effects. As can be seen in Fig. 3.7, changing Re while keeping Ca_o and Ca_i constant results in increase in the z -eccentricity. When Re is changed while not keeping the deformations constant, a decrease in eccentricity is possible. When that happens, the steady-state configuration that was previously shown in Fig. 3.5b is recovered. However, it is possible that the disappearances of revolving motion and drifting motion to be not linked, as will be discussed in Section 3.2.3.

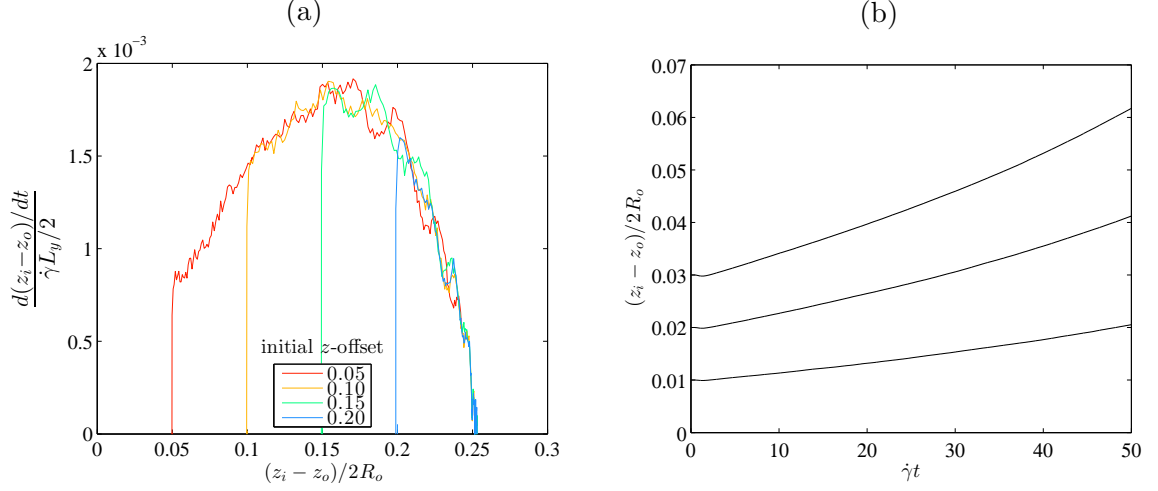


Figure 3.6. : (a) Phase portrait of dimensionless relative z -velocity versus position of the inner droplet. The inner drop is initially offset in the z -direction with the magnitudes indicated in the legend; (b) Dimensionless relative z -direction movement of the inner drop versus dimensionless time, given various initial offsets in the z -direction.

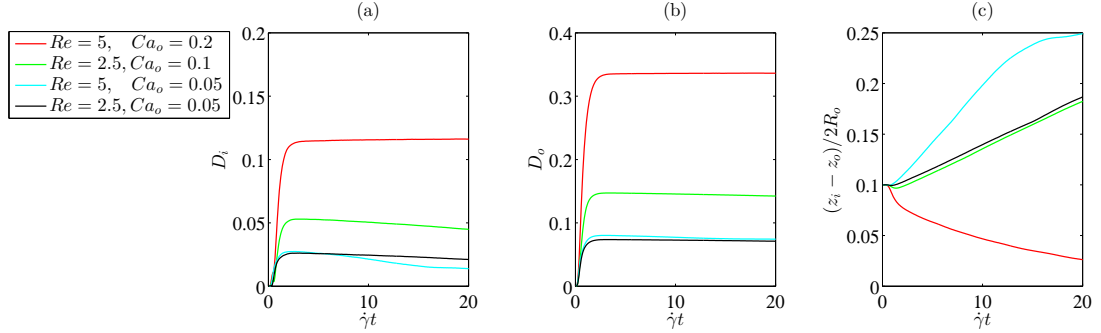


Figure 3.7. : The inertial effect on the drifting motion is investigated by increasing the shear rate with and without keeping Ca_o constant. Given an initial z -eccentricity, (a) D_i , (b) D_o , and (c) normalized relative z -position of the inner drop are shown. The reversal in the drifting motion with $Re = 5$ and $Ca_o = 0.2$ is due to a large deformation in the outer drop, as was the case in the revolving motion.

Combined motion

The natural extension of the revolving and drifting motions is to characterize if specific initial configuration dictates the final configuration of the inner droplet. Because having the inner droplet offset in either the x or the y direction results in the same limit cycle, whereas having z offset results in a completely different motion, we look at various eccentric inner droplet placements in the xz -plane.

The initial offset, outward migration path, and the final limit cycle behavior of the inner droplets are illustrated in Fig. 3.8. The initial positions are marked with filled triangles. The open diamonds within the migration paths are given at local x maxima for the xz -plane view and y maxima for the yz -plane view, and therefore represent the envelope that contain the revolving motion while drifting motion simultaneously takes place. The final local x -maximum and y -maximum, which are the global x -maximum and y -maximum, correspond to when no more outward motion is possible, *i.e.* the limit cycle, and are marked with filled circles. Unlike the case in a pure revolving motion, the limit cycle now contains an z -eccentricity. This method of viewing the migration leads to kinks in the yz -plane view, which is attributed to the distance between the initial position and the first local y -maximum.

The inner droplet almost comes into contact with the outer interface in the limit cycle at the y -extrema, but not at x -extrema. This fact is in accordance with Fig. 3.2b and Fig. 3.2d, and is also revealed when we look at the limit cycle trajectory for various offsets as shown in Fig. 3.9, as well as from the fact that the final y -offsets are larger than the x -offsets in Fig. 3.8.

The outward movement of the inner drop away from the center of the outer drop during the combination of revolving and drifting motions can be contrasted to what may happen to a point particle in a simple droplet. If the inner drop size were infinitesimal, the streamlines in Fig. 3.5a will be symmetric about the center of the outer drop (which is indeed the case for simple drop), and an outward motion is difficult to imagine. At best, if we imagine the drift movement of many point particles

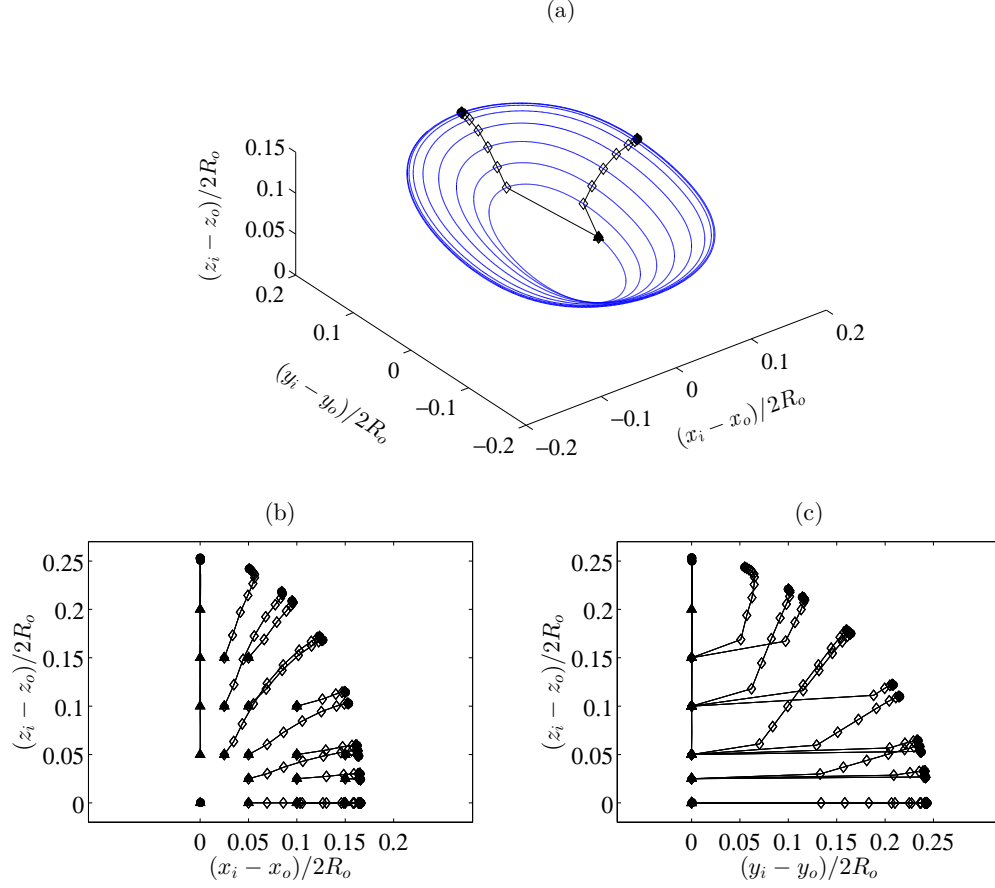


Figure 3.8. : Dimensionless (a) 3-D view of the migration path of the inner droplet initially placed at $(x, z) = (0.05, 0.05)$ with $k = 0.5$. The two black lines represent how the (b) xz -plane view and (c) yz -plane view are acquired when various initial eccentricities are tested. The initial positions are marked by triangles and the final by filled circles. The open diamonds denote the local maxima in (b) x and (c) y positions such that only the outward component of the motion is shown from the combination of revolving and drifting motions. The global maximum in x or y (*i.e.* envelope of the limit cycle) is shown with filled circles.

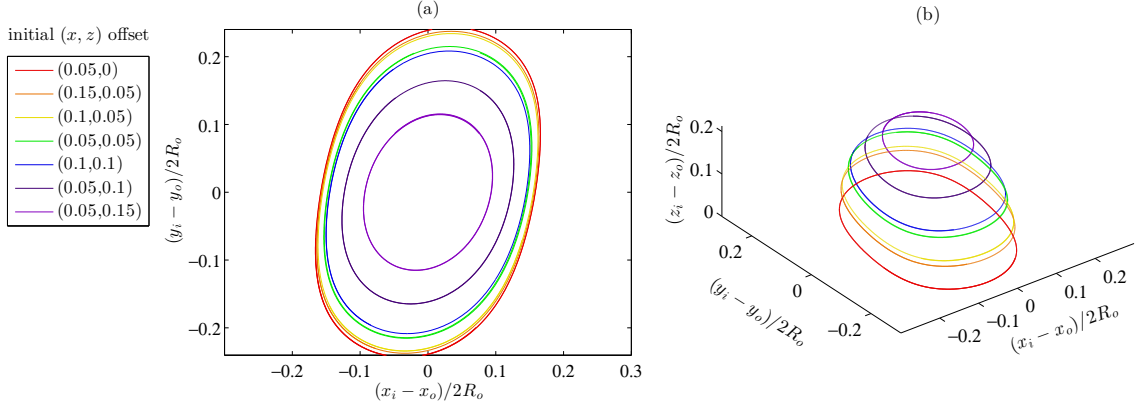


Figure 3.9. : (a) xy -projection and (b) 3D view of the limit cycle movement of the center of the inner droplet with various initial (x, z) offsets noted in the legend. The normalized relative position of inner droplet is plotted for ~ 1.5 revolving cycle, and show a tilted elliptical pattern.

within a simple droplet over time, because the fluid mass has to be conserved inside the said droplet, some point particles will move towards the center of the droplet if some moved outward. On the other hand, when we have inner droplet of finite size, we see that it only moves outward;

Another characteristic of the droplet migration is that the outward motion in the revolving motion happens with a timescale similar to that of the drifting motion. This is evident because the outward migration paths are approximately radial in Fig. 3.8. The similarities in the timescales can also be seen from Fig. 3.2a, 3.2c, and 3.2e; as previously stated, the increases in the envelope for relative x and y positions, and the increase in the relative z position occur over a timescale $\dot{\gamma}t \sim O(100)$.

3.2.2 Effect of radii ratio between inner and outer droplets

As demonstrated in Fig. 3.10, additional radii ratios of $k = 0.4$ and 0.6 are tested with various offsets. To prove that the outward migration into limit cycle is not dependent upon having the initial eccentricity confined to the xz -plane, the inner

droplets are placed in the yz -plane for the $k = 0.6$ case. Similarly to before, the filled triangles denote the initial positions and the filled circles the global maxima, with open diamonds the local maxima. The lower bound on the radii ratio of $k = 0.4$ is chosen to limit the parasitic current under 1% of the maximum velocity within the computational domain, and the upper bound is chosen to allow the testing of various inner droplet offsets. The radii ratio does not have an impact in the general migration behavior of the inner droplet; the inner droplet migrates such that the eccentricity increases until the limit cycle is reached.

3.2.3 Effect of interfacial tension coefficient on migration

The effect of inner interfacial tension on the inner droplet movement is considered. With $k = 0.5$, inner interfacial tension coefficients of $\sigma_i = 0.2 - 2.0$ are tested, corresponding to $\beta = 0.1 - 1$ and $Ca_i = 0.25 - 0.025$. As shown in Fig. 3.11, a decrease in β corresponds to a lower migration speed of the inner droplet. Whereas the decrease of β from 1.0 to 0.6 barely affects the overall movement of the inner droplet, the decrease from 0.4 to 0.2 greatly reduces the migration velocities in all the tested cases.

In the case of the revolving motion, a decrease in β from 0.2 to 0.1 results in a reversal in the outward movement. This behavior is similar to that observed in 2D simulations by Hua *et al.*, who chose $Ca_i = 0.25$ and observed that the inner droplet drifted to the center of the outer droplet regardless of the initial eccentricity.

The drift velocity in the z -direction depends weakly on σ_i ; there is no reversal in the drift motion with a change in σ_i . Further, a decrease in β from 1 to 0.6 has negligible effect on the drift velocity. It is only when the inner drop deformation grows significantly that the drift velocity noticeably decreases.

When $0.025 < Ca_o < 0.1$, revolving motion is suppressed when $Ca_i = 0.25$ but drifting motion is always observed, as shown in Fig. 3.12; whereas the revolving motion is suppressed for critical $Ca_i = 0.25$ and $Ca_o = 0.2$, the drifting motion persists

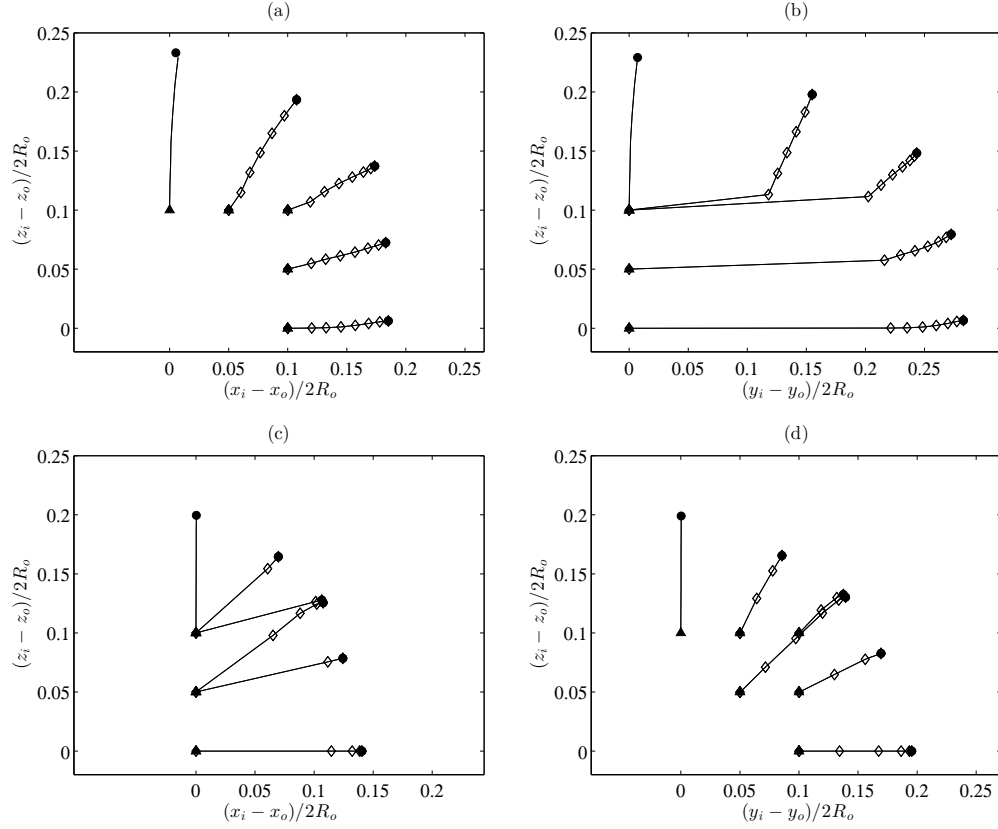


Figure 3.10. : Behavior of the inner droplet depending on the initial inner droplet placement and the radii ratio. Dimensionless (a) xz -plane view and (b) yz -plane view with the inner droplets initially placed with various (x, z) offsets with $k = 0.4$; dimensionless (c) xz -plane view and (d) yz -plane view with various (y, z) offsets with $k = 0.6$. Filled triangles, filled circles, and open diamonds are used in the manner similar to Fig. 3.8, and familiar outward migrations to when $k = 0.5$ are observed.

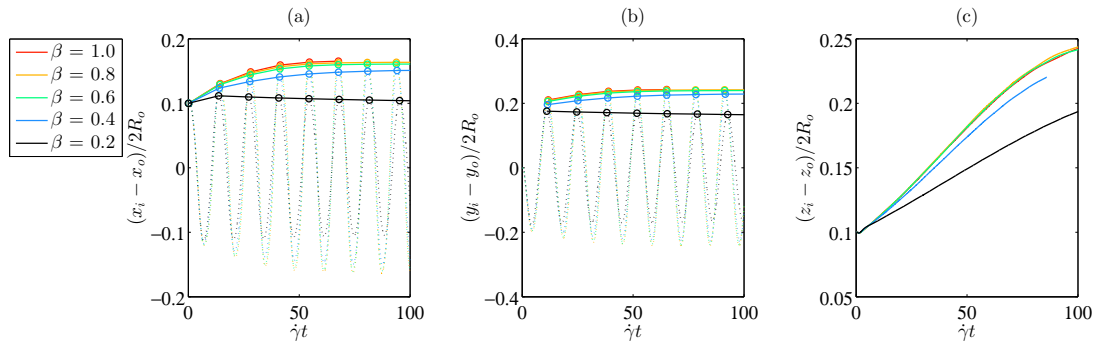


Figure 3.11. : Dimensionless relative position of the inner droplet versus dimensionless time with various β . Normalized relative (a) x and (b) y positions are shown with dotted lines, with initial inner drop offset in the x -direction. The maxima in x and y positions are marked with circles and are connected; (c) normalized relative z -position is shown with initial inner drop offset in the z -direction.

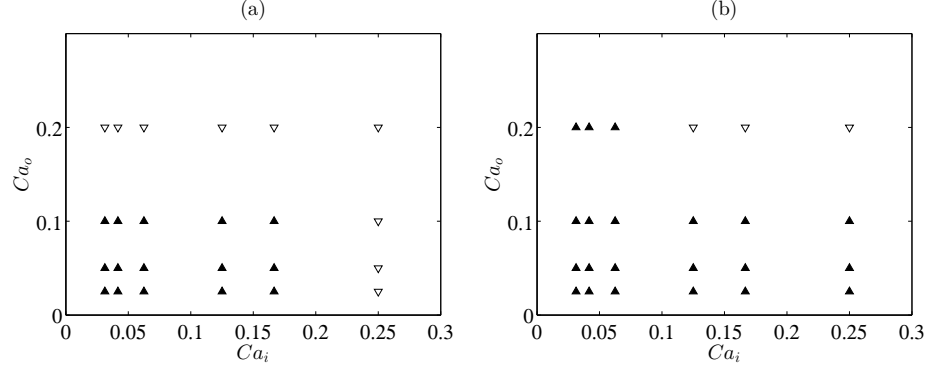


Figure 3.12. : The increase (filled upward triangle) and decrease (open downward triangle) of eccentricity in the Capillary number space with initial (a) x and (b) z eccentricity.

for a wider range of capillary numbers. On top of the effect of capillary numbers, the initial configuration must also be considered: the creation of recirculation zones in Fig. 3.5b does not always occur with an almost-spherical inner drop and initial z -asymmetry, and thus even with $Ca_o = 0.2$, drifting motion can persist. This difference in the critical capillary number at which revolving and drifting motions are suppressed suggests that a more complicated combined motion is possible, where the inner drop may no longer migrate radially outward. For example, when $\beta = 0.1$ and $Ca_o = 0.05$, the movement of the inner drop is characterized by the suppression of revolving motion, and when $\beta = 0.2$ by the suppression of drifting motion depending on the initial configuration. This is shown in Fig. 3.13.

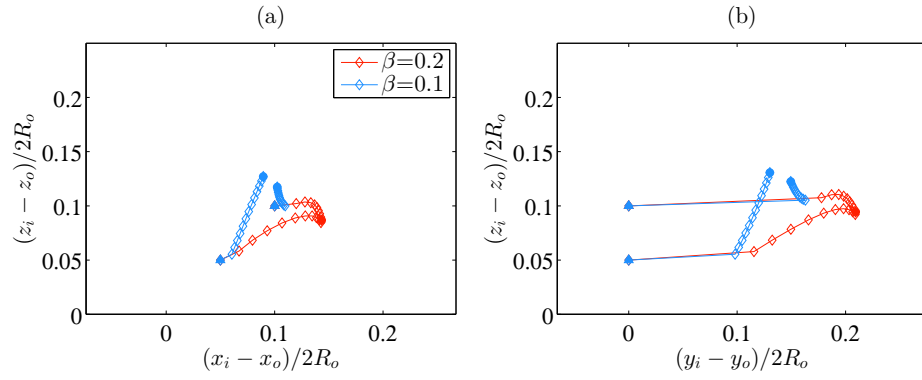


Figure 3.13. : Comparison between $\beta = 0.1$ and $\beta = 0.2$ with initial (x, z) offsets of $(0.05, 0.05)$ and $(0.1, 0.1)$ with $Ca_o = 0.5$. Dimensionless (a) xz -plane view and (b) yz -plane views are shown in identical manner to Fig. 3.8 and Fig. 3.10. While the inner drop still moves away from the center of the outer droplet, the outward motion is no longer radial.

4. LATERAL MIGRATION DOUBLE EMULSION DROPLETS IN LOW REYNOLDS NUMBER POISEUILLE FLOW

In this chapter, we consider the lateral migration of compound drops in a three-dimensional Poiseuille flow within a rectangular channel. In the low Reynolds number regime ($Re = O(1)$) with equal and uniform viscosity and density, 4 equilibrium configurations are found. These equilibrium configurations are realized by releasing initially concentric compound drops with varying radii ratio between the inner and outer drops at different locations within the channel. The different internal streamlines in each equilibrium configuration are discussed. Additionally, whether a given initial configuration leads to a steady state or not due to the interfaces merging is discussed. Finally, the effect of initial compound drop placement, the effect of size ratio of the compound drop relative to the channel, and the effect of aspect ratio of the channel are considered.

4.1 Problem Statement

We consider the trajectory and the steady-state equilibrium location of a compound drop with a single inner drop. The compound drop is initially concentric with an undeformed outer radius R_o and inner radius R_i . The initial condition is zero velocity in the channel. A constant pressure gradient drives the flow in the channel. The channel has a rectangular cross-section of $(L_y/(2R_o) \times L_z/(2R_o)) = (1.5 \times 2.5)$, and is periodic in the flow direction with $L_x/(2R_o) = 2$. The schematic is shown in Fig. 4.1. The initial placement of the center of the compound drop is $y/L_y \leq 0.5$ and $z/L_z \leq 0.5$. Initial positions with $y/L_y > 0.5$ or $z/L_z > 0.5$ are not considered due to symmetry. The density ρ and viscosity μ of all fluids are equal and uniform, and the interfacial tension coefficient at the inner and outer interfaces are equal and uniform.

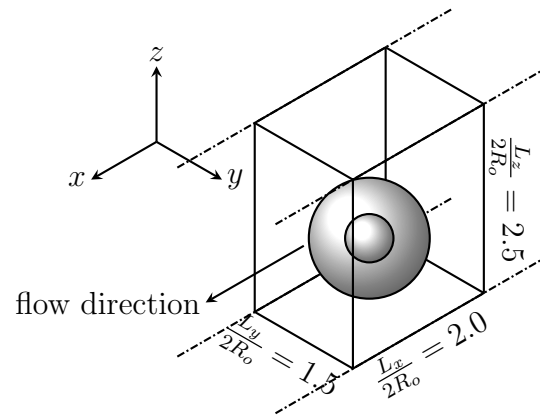


Figure 4.1. : Schematic of the computational domain. A spherical and concentric compound drop is placed in a pressure driven channel. The channel initially has zero velocity and the flow is in the x -direction.

Here, the computational domain is resolved using $64 \times 48 \times 80$ or $128 \times 96 \times 160$ grid points, corresponding to 16 or 32 grid points across the diameter of the undeformed inner drop, respectively. The coarser grid is used by default, and the refined grid is used to verify the coarse grid simulations when a small change in the initial compound drop placement results in different equilibrium configurations at steady state. The computation is stopped either when an equilibrium is reached or when the inner and outer interfaces come within 1% of initial outer drop diameter, corresponding to half of refined grid spacing and thus indicating a breakup of the compound drop.

4.2 Results and Discussions

4.2.1 Equilibrium Configurations

Four equilibrium configurations - centerlined, single vortex, pair vortex (outer), and pair vortex (inner) - are found, where the latter three are named depending on the number of vortices inside the compound drop at the bisecting plane of symmetry, and depending on where the inner drop is relative to the channel centerline.

All equilibrium configurations, streamlines in the reference frame of the outer drop, and flow direction averaged velocity profile are shown in table 4.1. Single vortex equilibrium is the most common one when all initial placements are considered. One exception is when the initial placement is symmetric about the longer wall, in which case the pair vortex (outer) equilibrium is reached. For a given equilibrium configuration, the flow direction averaged velocity profile is nearly identical regardless of the radii ratio. Each equilibrium is further described in the following.

The centerlined equilibrium configuration is reached when a concentric compound drop is initially placed at the channel centerline. The inner drop migrates along the flow direction faster than the outer drop, and reaches the front side of the outer drop as expected. The counter-rotating vortices inside the inner drop qualitatively agree with streamlines shown by Che *et al.* [70] despite slightly different Ca and significantly

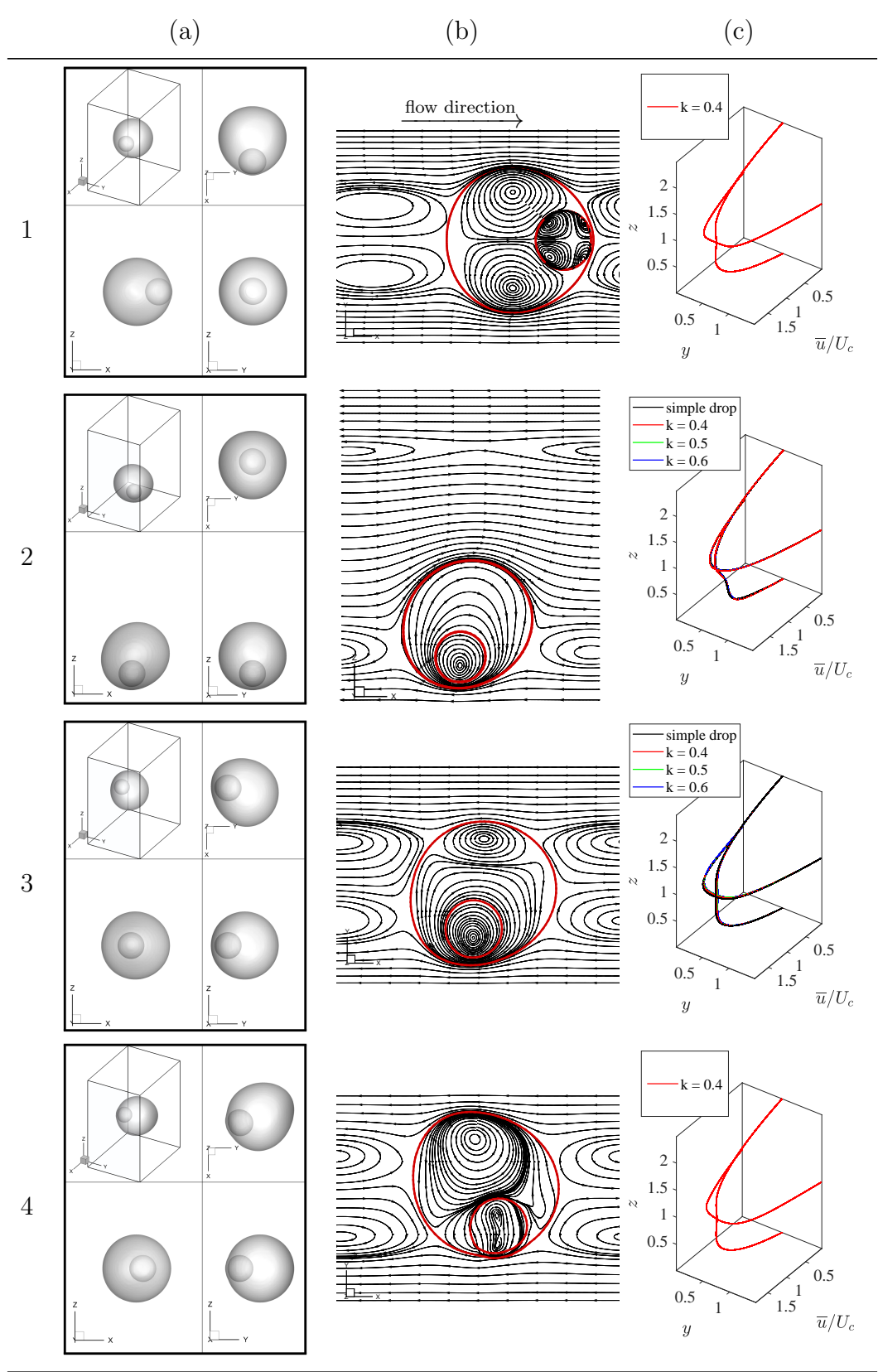


Table 4.1. : (a) Equilibrium configurations, (b) streamlines at channel midplane (xz or xy plane) in reference frame of outer drop with flow to the right, and (c) normalized flow direction averaged velocity profiles for (1) centerlined, (2) single vortex, (3) pair vortex (outer), and (4) pair vortex (inner) equilibria.

different Re . This configuration is metastable and is prone to drop breakup as well as migration away from centerline with accumulation of numerical error.

In the single vortex equilibrium, the compound drop is close to the shorter side of the channel. This equilibrium and the streamlines inside the outer drop are similar to those at the “outer equilibrium position” reported by Chen *et al.* [43], who investigated the equilibria of simple drops in a 3-dimensional rectangular channel. A well defined single vortex exists and encircles the periphery of the inner drop. The compound drop does not intersect the midplane that bisects the longer side of the channel. An analogous equilibrium to the “inner equilibrium position” reported by Chen *et al.* is not found for compound drops with the current Re . A general compound drop placement results in this stable equilibrium.

The pair vortex (outer) equilibrium is reached when the initial compound drop placement is symmetric about the longer wall (the z -direction). This symmetry (and hence this equilibrium) is metastable. In the case of a simple drop, counter-rotating eddies are present when the drop intersects the centerline [71], and similar streamlines are present inside the compound drop in this configuration. The counter rotating eddies are not toroidal and are of different sizes, with the larger eddy circulating about the inner drop. The inner drop is near the channel wall (away from the centerline, hence the term “outer”) compared to the pair vortex (inner) equilibrium.

Unlike in the pair vortex (outer) equilibrium, the smaller eddy circulates around the inner drop in the pair vortex (inner) equilibrium. In the pair vortex (inner) equilibrium, the inner drop is placed further away from the channel wall and closer to the centerline. This equilibrium is not found for $k \geq 0.5$ for the given flow parameters at hand. When compared against the streamlines in the xy -plane view for the pair vortex (outer) equilibrium, the larger counter rotating eddy in pair vortex (inner) equilibrium is more deformed, and the smaller counter rotating eddy now has a figure 8 which is due to the toroidal vortex inside the inner drop. The final outer drop’s centroid y -position of $y_o/L_y = 0.575$ means that the outer drop’s final centroid position is a mirror image of that in the pair vortex (outer) equilibrium, which has $y_o/L_y = 0.425$. This equilibrium

configuration is metastable similarly to the pair vortex (outer) configuration. However, whereas pair vortex (outer) configuration may be reached without the interfaces coming into contact, this configuration cannot be reached starting with a concentric compound drop in a quiescent domain. Instead, this equilibrium is reached when the interfaces are explicitly constrained to not merge or break; following a numerical error accumulation and the subsequent symmetry breaking from the centerline equilibrium, the inner drop experiences a larger migration force along the y -direction than the z -direction due to the larger velocity gradient from the shorter channel length, and the compound drop transitions to the pair vortex (inner) configuration.

4.2.2 Effect of Initial Placement on Stability

The effect of the initial placements on the equilibrium configuration has been briefly described. In microfluidics engineering, compound drops are often generated using a pinch-off devices and then are accumulated soon after. A situation may rise where such accumulated compound drops need to be transported again. In such a scenario, the external flow experienced by compound drop changes from quiescent to pressure driven, and the integrity of compound drop to overcome breakup is an important question.

To further investigate the effect of radii ratio and initial placements, we look at their effects on the breakup time as shown in Fig. 4.2. As described previously, the compound drop is considered to undergo breakup when the inner and outer interfaces come within 1% of the initial outer drop diameter, and the breakup time is the time from the start of the simulation to when the breakup occurs. If the compound drop reaches the equilibrium location without breaking up, then the compound drop is considered stable.

Fig. 4.2 also shows the inner drop movement (in red) and the outer drop movement (in black) for various initial placements. The initial movement of the inner and outer drops are in opposite directions, after which a damped oscillatory movement from the

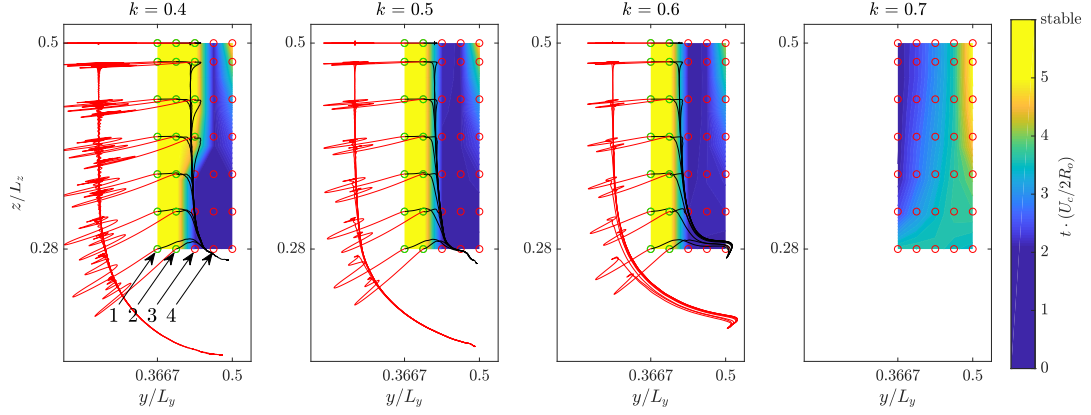


Figure 4.2. : The effect of radii ratio and initial placements on the drop stability and migration paths are shown. Green circles denote initial placements that do not result in breakup and red circles denote initial placements that do. Black paths denote outer drop centroid movement and red inner. Migration paths associated with initial placements that result in breakup are not shown. The color contour shows the time of breakup. Only a portion of the channel is shown to scale to clearly show the migration paths.

inner drop follows similarly to observed in compound drops in simple shear flow [72]. The inner drop movement is far greater than outer drop movement, and so the breakup time of the compound drop is largely dictated by the inner drop dynamics.

In general, the smaller the radii ratio, the longer the compound drop takes to breakup. The near-wall initial placements is effective at preventing breakup. There exists a small region near the centerline where the compound drop does not break up for some time, but no region near the centerline is found to be completely prevent breakup. The stability of near-wall region is further looked at as shown in Fig. 4.3 by focusing on 4 cases with $k = 0.4$ as denoted in Fig. 4.2.

In those four cases, the distance between the inner and outer drop reaches a similar value of 0.3 when normalized by $(2R_o)$. However, the deformation experienced by

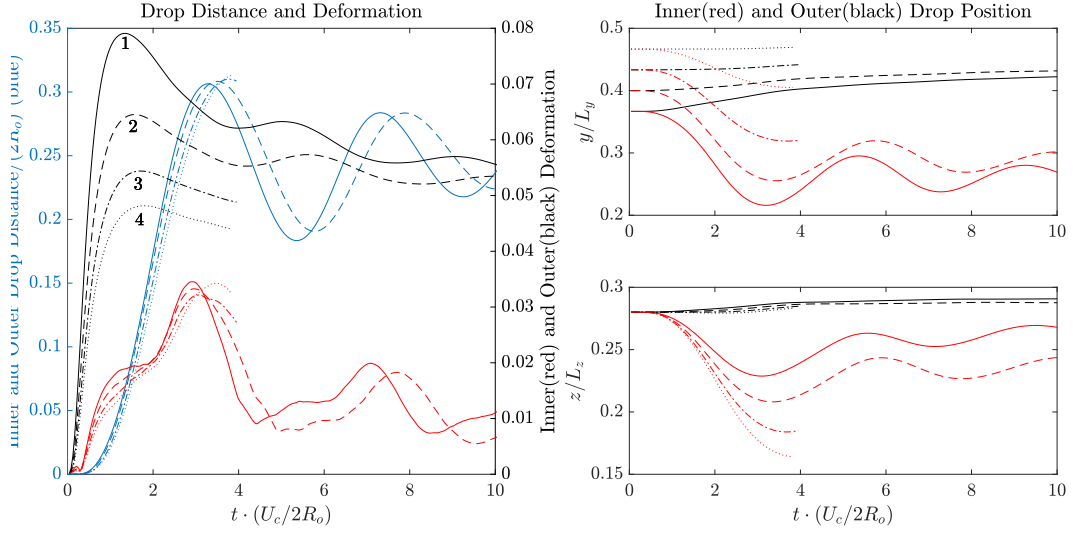


Figure 4.3. : Cases 1 through 4 denoted in Fig. 4.2 are more closely looked at. Distance between inner and outer drop centroids (blue), inner (red) and outer (black) drop deformations are shown on the left. Inner (red) and outer (black) drop movements in y and z direction are shown. Cases 3 and 4 are shown until breakup.

the outer drop differs significantly, since the effective shear gradient at those different locations are different. This in turn allows or limits the space that the inner drop may settle into; that is, an outer drop with larger deformation is able to accommodate the oscillatory inner drop movement that is expected from the effective shear gradient, whereas an outer drop with a smaller deformation cannot. The deformation of the inner drop are similar and does not play a big factor. The fact that inner drop movement is the major factor in determining the distance between the inner and outer interfaces is shown in Fig. 4.2 as well when we compare the magnitude of movement in the outer and inner drops over time.

The fact that Taylor deformation number of the outer drop reaches a value as high as 0.08 despite having the Capillary number of the system being $O(0.1)$ warrants an explanation. Oftentimes the deformation number is used to characterize the dynamics in a simple shear flow, where the Capillary number is defined based on the velocity due to the effective shear across the overall drop. If we look at the effective Capillary number in positions 1 through 4 in Fig. 4.2 as defined by the effective shear the outer drop undergoes, the value is 2 to 3 times greater than that defined by the channel average velocity U_c .

4.2.3 Effect of Geometric Parameters on the Equilibria

The effects of geometric parameters on the equilibrium positions and average channel velocity are considered. Although the single vortex equilibrium is more likely to occur for an arbitrary initial compound drop placement, both single and pair vortex equilibria are considered.

Effect of Size Ratio of Compound Drop to the Channel and Radii Ratio of Compound Drop

Droplet sorting by size has been demonstrated with great accuracy in microfluidics by the usage of bifurcating geometries [73]. To extend such a knowledge to compound

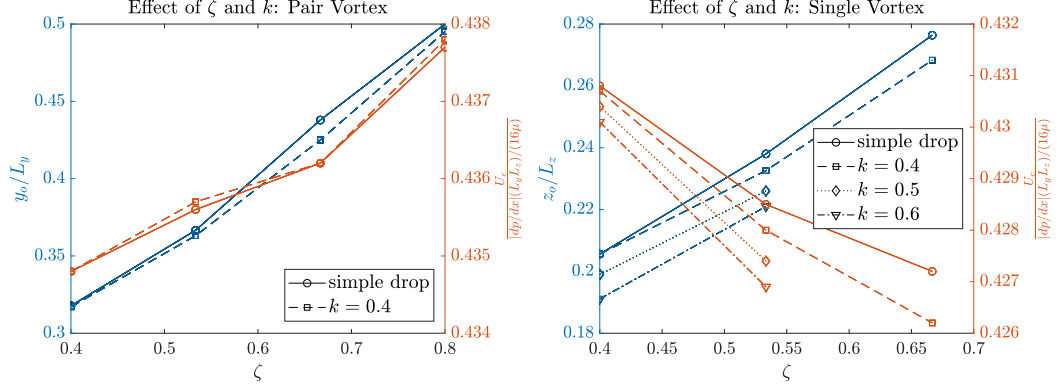


Figure 4.4. : The effect of size ratio of the compound drop to the channel and the radii ratio of the compound drop on the equilibrium position and the channel throughput.

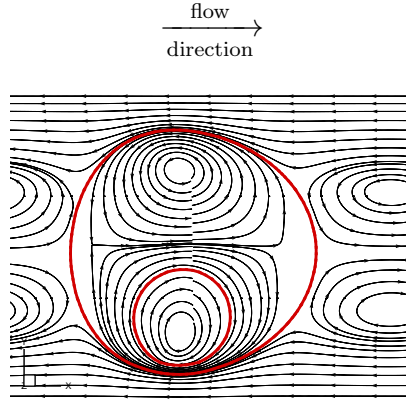


Figure 4.5. : Streamlines in the xy -plane view at the z -midplane with $\zeta = 0.8$. Pair vortex (outer) equilibrium is reached, but the significant wall effects position the compound drop at the center of the channel.

drops, the effect of size ratio is considered by changing R_o while maintaining the channel size constant and scaling R_i for a desired k . The dimensionless equilibrium positions and the dimensionless channel average velocity are shown in Fig. 4.4.

As ζ increases, the dimensionless equilibrium position also increases for both pair vortex and single vortex equilibria. For the pair vortex equilibrium, As ζ approaches

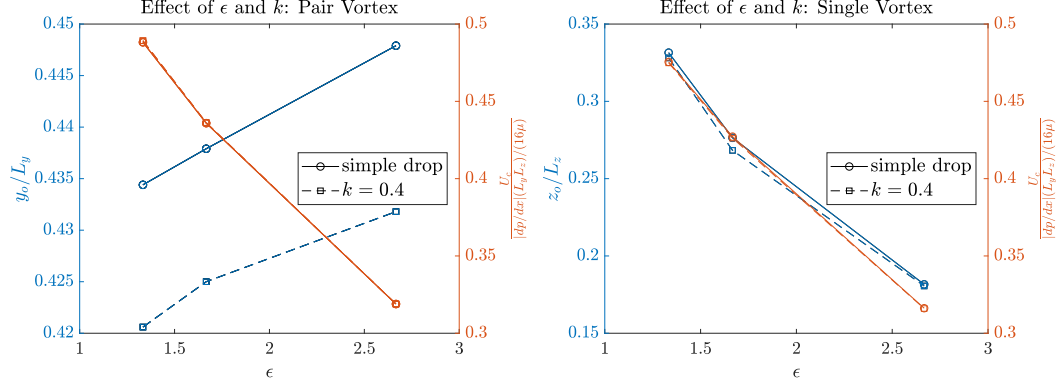


Figure 4.6. : The effect of channel aspect ratio on the equilibrium positions of simple and compound drops, and on the channel throughput.

0.8, the compound drop does not reach the equilibrium that was previously described. Instead, it reaches an equilibrium that is a mixture of centerlined and pair vortex (outer) equilibria as shown in Fig. 4.5. In this equilibrium, the wall effects position the outer drop at a centerlined position, and the inner drop is placed within one of the counter rotating vortices within the outer drop.

Additionally, an increase in k brings the compound drop closer to the channel wall and also decreases the average channel velocity. The average channel velocity increases with ζ for pair vortex equilibrium, but decreases for single vortex equilibrium. The change in the average channel velocity is very small.

Effect of Channel Aspect Ratio

In production and application of compound drops such as in microfluidic devices, the cross section of the channel is often restricted in one direction, and increasing the throughput of the channel is achieved by changing its aspect ratio rather than scaling the channel as a whole. In this light, we consider the effect of increasing the aspect ratio of the channel by elongating L_z , and look at the equilibrium position and the channel throughput as shown in Fig. 4.6.

The nondimensional channel throughput between simple drop and compound drop look nearly identical. This is due to how the average channel velocity is nondimensionalized; since L_z is in the denominator of the nondimensionalization, small changes in the throughput is overshadowed by the large changes in L_z between each case.

On the other hand, the positional difference between a compound drop and a simple drop can easily be seen, and shows a similar trend as the effect due to the size ratio; the compound drop's equilibrium position is closer to the channel wall than that of the simple drop. For the single vortex equilibrium, the nondimensional equilibrium position is misleading in that z_o/L_z is decreasing with increase in the channel aspect ratio, but the actual equilibrium position z_o increases with ϵ .

5. CROSS STREAM LIFT FORCE ON A COMPOUND DROP IN 3D RECTANGULAR POISEUILLE FLOW

We considered the equilibrium configurations and positions of compound drops in Poiseuille flow in the last chapter. But we also saw that the equilibrium positions of compound drops are very close even with varying radii ratio, and even against simple drops. Hence, an efficient sorting is a difficult task. In this chapter, we look at the lift force profile of compound drops and simple drops at varying placements within the same channel. It will be shown that the lift force profile varies significantly with radii ratio in the inner region of the channel, thus opening possibilities of forced sorting mechanism (through the application of external force field such as an electric field) or temporal sorting mechanism (since the different compound drops with different radii ratios will laterally migrate at different rates). Finally, we will discuss the model for explaining why the different in the lift force arises, and also discuss the limitations of the model.

5.1 Problem Statement

We computationally consider the lateral lift force acting upon a compound drop at its steady state. The compound drop is initially concentric with an undeformed outer radius R_o and inner radius R_i . The initial velocity within the channel is parabolic, and the velocity field eventually reaches steady state under a constant pressure gradient along the flow direction. The rectangular channel has a cross section of $L_y/(2R_o) = 1.5$ and $L_z/(2R_o) = 2.5$, and has the periodic length along the flow direction of $L_x/(2R_o) = 2.0$. The computational domain schematic is shown in Fig. 5.1.

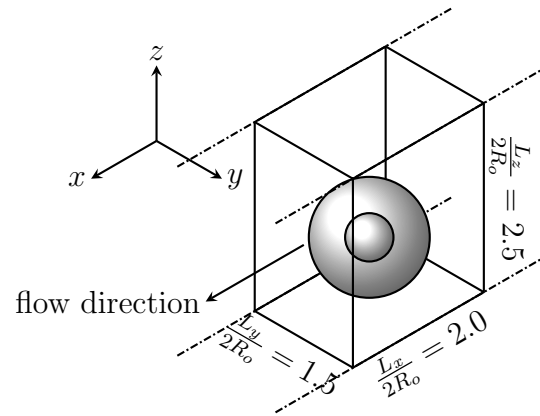


Figure 5.1. : Schematic of the computational domain. A spherical and concentric compound drop is placed with symmetry about y , the short wall direction. Various compound drop placements along z , the long wall direction, is considered. The flow is initially parabolic, and is pressure driven in the x -direction.

We've shown in the previous chapter that compound drop placements without symmetry about the long channel direction lead to the single vortex equilibrium when channel Reynolds number is $Re = O(10)$ and drop capillary number is $Ca = O(0.1)$ [74]. Since the symmetry about the short wall direction is more strongly enforced than that about the long direction, the lateral lift force along the long channel direction determines how the compound drop laterally migrates as it is carried along the flow. Hence, the initial placements for finding the lift force on the compound drops have symmetry about the short wall direction, and are spread across the lower half of the channel. That is to say, $y_o/L_y = 0.5$ and $z_o/L_z \leq 0.5$ initially.

To determine the lateral lift force acting on the compound drop, we use a PI controller similar to one employed by Schaaf and Stark [75]. An adjustable force F_b is applied evenly throughout the volume of the compound drop, which compensates the lift force. This feedback force is calculated with a proportional term and an integral of the error term. At some time t , the current position of the outer drop $z_o(t)$ can be compared against the desired and initial z -position of the outer drop $z_o(t = 0)$ to acquire the proportional term. The error of this term is then integrated over time for a faster convergence of the compound drop position and hence the lift force. The feedback force is calculated as

$$F_b(t) = \gamma_P(z_o(t = 0) - z_o(t)) + \int_0^t \gamma_I (z_o(t = 0) - z_o(t')) dt', \quad (5.1)$$

where the values of γ_P and γ_I are in the range of $0.1 - 5$ and $10 - 50$ depending on the case for good convergence of the PI controller. The found F_b is then applied along the z -direction, and the lift force is found as $F_L = -\int_{\text{Vol}} F_b dV$, where the volume integral is over the entire volume of the compound drop. While this lift force is applied throughout the compound drop, and hence both the inner drop and outer drop experience the lift force, only the outer drop location is constrained by the PI controller. A merging of the interfaces is possible since the inner drop is free to move inside the outer drop cavity. The computations are stopped when the inner interface and outer interface come within half a grid spacing, *i.e.* $R_i/16$. In the cases where the interface merging occurs before the convergence of the PI controller, the final four

local minima and maxima of the lift force are extrapolated to obtain the projected lift force. The cases where such extrapolation is required are clearly labeled in the results section.

We focus on the Reynolds number based on the hydraulic diameter H as $Re = \rho U_c H / \mu = 9.6$ and capillary number of $Ca = \mu U_c / \sigma = 0.1$. Additionally, we vary the the outer drop viscosity so that $\mu_{\text{new}} / \mu_{\text{old}} = 1/2$ or 2 to show that the lift force is affected far more greatly by radii ratio $k = R_i / R_o = 0.4 - 0.6$ rather than the viscosity ratio. Finally, a few cases with Ca ranging up to $O(1)$ are discussed to aid in designing predictable compound drop delivery system without breakup occurring.

5.2 Results and Discussion

The lift forces found with the PI controller are labeled as F_L and act in the positive z -direction. The lift forces are then nondimensionalized against $\rho U^2 a^4 / H^2$ where U is the maximum channel velocity, a is the diameter of the undeformed outer drop (or simple drop), and H is the hydraulic diameter of the channel. This nondimensionalization is in accordance with Asmolov [76], who predicted an increase of the nondimensional lift force f_L with decreasing Reynolds number. Although that prediction was made for a much larger Reynolds number than here, we see that it holds even in the current system as shown in Fig. 5.2.

5.2.1 Effect of Radii Ratio on Lift Force

The most important aspect of the lift force profile is if there is a noticeable difference between that of a simple drop and a compound drop. As shown in Fig. 5.3, there is. We first note that the lift force profile of a simple drop behaves similarly to the particle result by Di Carlo *et al.* [77] and capsule result from Schaaf and Stark [75]. But in the channel center region (*i.e.* away from the near wall region), the compound drops show significantly more lift force. Furthermore, this trend is accentuated for a larger radii ratio k . While the equilibrium position, as predicted by when the lift

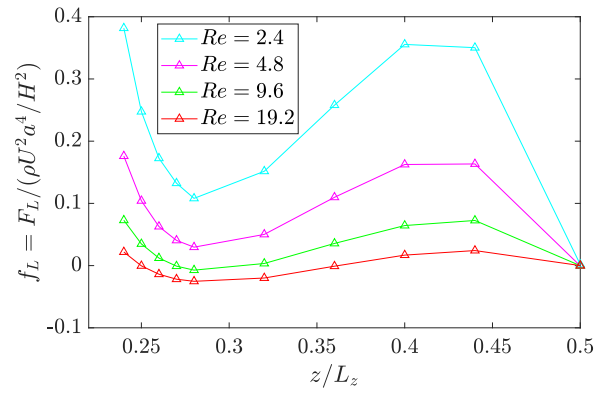


Figure 5.2. : The nondimensional lift force on a compound drop with various positions $z_o/L_z \leq 0.5$ with radii ratio $k = 0.6$. The Reynolds number is varied from 2.4 to 19.2.

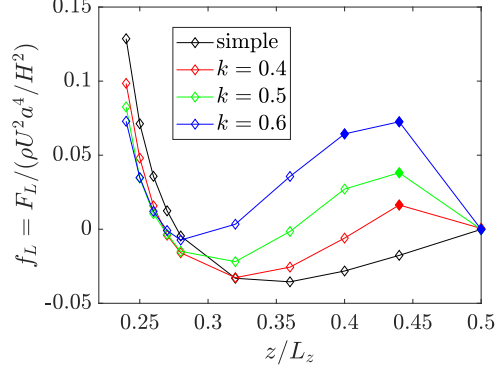


Figure 5.3. : The nondimensional lift force on simple and compound drops with various positions $z/L_z \leq 0.5$ and varying radii ratio $k = 0.4 - 0.6$. The hydraulic Reynolds number is 9.6. The filled in markers imply extrapolation as previously described.

force is 0, between all the cases are very similar, the big difference in the lift force in the inner region can aid in sorting of the compound drops based on the radii ratio by means of external forcing (such as through electric field) or by temporal means (since the compound drops will laterally migrate at a different rate than simple drops or compound drops with different radii ratio).

One interesting thing to note is the equilibrium at the centerline. The curvature on the lift force profile of the simple drop predicts that $z/L_z = 0.5$ is an unstable equilibrium. On the other hand, the compound drop lift force profiles predict that the centerline is a stable equilibrium. However, from the previous work, we've shown that the centerline equilibrium is not desirable in the sense that the inner interface merges with the outer interface [74]. This fact is shown in Fig. 5.3 for the near-centerline placements with the filled markers, implying that interface merging does occur.

5.2.2 Effect of Outer Drop Viscosity on Lift Force

Oftentimes in the application of compound drops, the inner drop and surrounding fluid have similar fluid properties while the outer drop has a very different property.

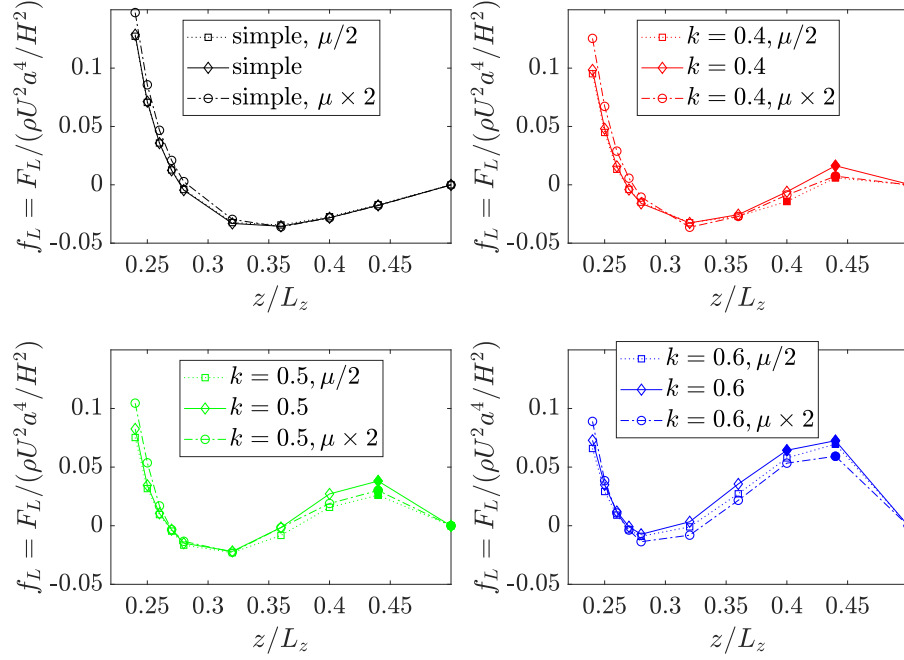


Figure 5.4. : The nondimensional lift force on simple drop and compound drop with various positions $z/L_z \leq 0.5$ and varying radii ratio $k = 0.4 - 0.6$. The hydraulic Reynolds number is 9.6. The simple drop viscosity and outer drop viscosities are varied as $\mu_{\text{new}}/\mu_{\text{old}} = [1/2, 1, 2]$. The filled in markers imply extrapolation.

This also implies that the inner and outer interfaces have similar interfacial tension coefficients. With this in mind, we look at the lift force profiles when the outer drop viscosity is decreased or increased. The results are contrasted against simple drop whose viscosity also is decreased or increased, as shown in Fig. 5.4. The viscosity change in the outer drop affects the lift force far less than a change in the radii ratio. Hence, the geometry of the compound drop is a far greater factor in determining the lift force than the viscosity ratio between the phases. Interestingly, the lift force in the inner region of the channel is at the highest when all the phases have the same viscosities. This fact is very pronounced in the compound drops, while not so evident in the simple drop.

5.2.3 Discussion on Stable Compound Drop Control Design

We've shown in Fig. 5.3 that higher k results in higher lift force. This aids in lift-force-based separation and hence is desirable, but we've also shown that higher k is more likely to lead to breakup. For a compound drop control scheme to be useful, breakup must be delayed.

In a previous publication, we've shown that compound drops in simple shear flow can either stabilize (with the inner drop moving towards the center of the outer drop) or destabilize (with the inner drop moving towards the periphery of the outer drop) depending on the capillary number. The bifurcation occurs at $Ca_o \sim 0.2$ and $Ca_i \sim 0.2$, with higher Ca (and hence higher deformation) corresponding to stabilization.

The relevance of simple shear result is that the breakup dynamics can be controlled through manipulating Ca . The capillary number in a simple shear flow is defined in terms of the shear gradient across the compound drop, and does not directly translate to how it is defined in this work. However, the same Taylor deformation number gives a good measure of comparison [62]. Taylor deformation number can be calculated from the aspect ratio of drop, which in turn can be calculated from the second moment of inertia tensor for small deformations [60,61].

The capillary number of the inner and outer drops are changed by decreasing the interfacial tension coefficient of the inner and outer interfaces by up to 8 times as shown in Fig. 5.5. The deformation of the outer drop reaches a value that results in stabilization in simple shear flow at $4 \times Ca_{old} = 0.4$, and easily exceeds it near the wall with $8 \times Ca_{old} = 0.8$. The stabilization of the inner drop in pressure driven flow, despite such large deformations, is not as pronounced as it is in simple shear flow. The inner drop remains eccentric, although the eccentricity does not increase with time.

Nonetheless, increasing Ca results in larger distance between the interfaces, thereby stabilizing the compound drop. Moreover, the lift force profile in the near-centerline region of the channel is hardly affected. Changing Ca hence provides an effective

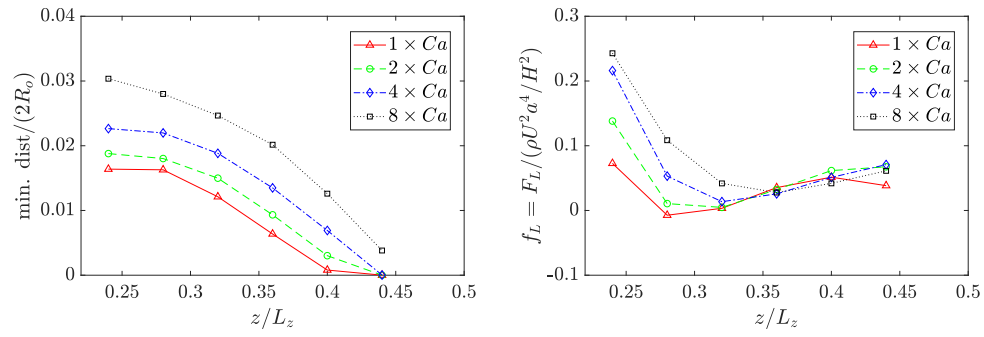


Figure 5.5. : (Left): The nondimensional minimum distance between inner and outer interfaces with varying Ca_o with $k = 0.6$ and (right): the corresponding lift force profile.

way of stabilizing compound drops as they are being sorted by difference in lateral lift force, while not significantly altering the lift force difference that exists in the near-centerline region due to difference in k .

5.2.4 Discussion on the Origin of the Lift Force

There are a few known contributions to the lateral lift force. These contributions are particularly well known for a small spherical particle. Namely, the Magnus force and the Saffman force are well documented. In a finite domain, the wall-induced lift force plays a key role when a particle or a drop is in the vicinity of a channel wall. For a deformable drop, the deformation also acts to influence the lift force. Finally, the curvature of the undisturbed fluid velocity also manifests as the shear gradient lift force, which acts to push the particles or drops towards the walls [78].

In this subsection, we aim to focus on the qualitative contribution of the deformation induced lift force, Magnus force, and Saffman force so as to discuss why the lift force profile of compound drops are different than that of a simple drop.

Deformation Induced Lift Force

When compared against a nondeforming particle, a deformation induces a lift force towards the center of the channel [78]. When we look at the Taylor deformation of the simple drop and outer drops as shown in Fig. 5.6, we see that the deformation is smaller the larger the inner drop, except for the near-centerline region. Since the near-centerline region relies on extrapolated from the not fully converged PI controller, we will focus more in the range $0.3 < z/L_z < 0.4$. In this region, the lift force is higher the larger the radii ratio. This trend, which is the opposite of what is expected, suggests that deformation induced lift force is not a major contributor to the difference in the lift force profile of compound drops.

Furthermore, when we look at the deformations with varying viscosities as shown in Fig. 5.7, the suggestion that deformation induced lift force is not a major contributor

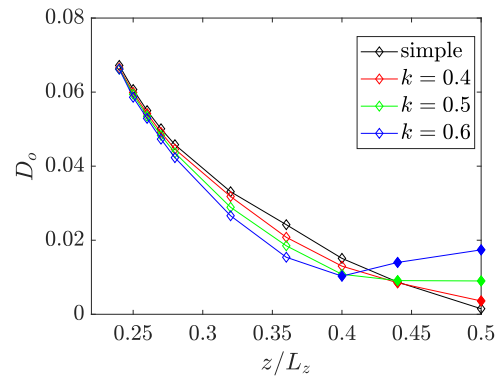


Figure 5.6. : The nondimensional simple drop or outer drop Taylor deformation of a simple drop or compound drops with varying radii ratio. The filled markers imply extrapolated deformation.

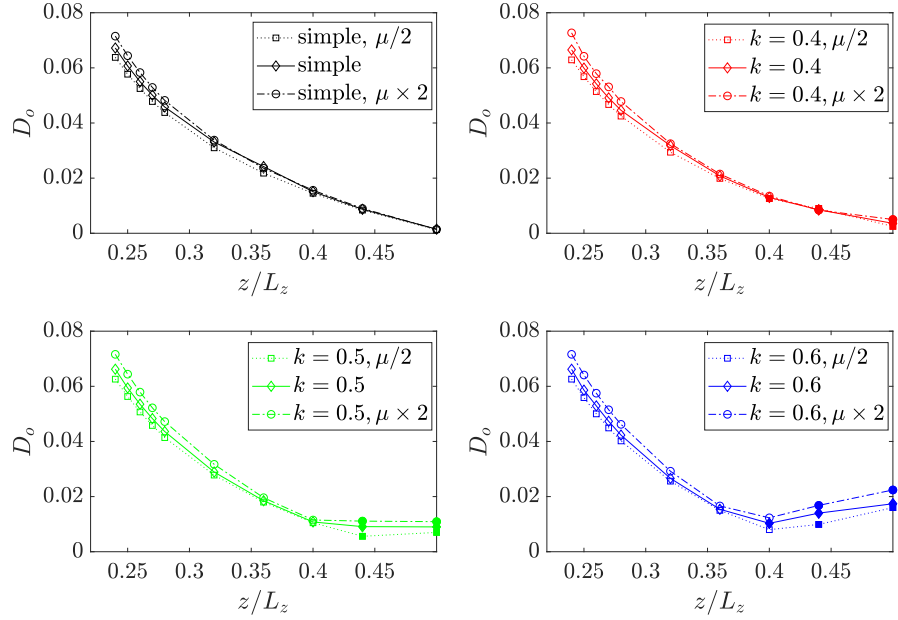


Figure 5.7. : The nondimensional Taylor deformation of a simple drop and compound drops with varying radii ratio. The viscosities of simple drop or outer drop are varied as $\mu_{\text{new}}/\mu_{\text{old}} = [1/2, 1, 2]$. The filled markers imply extrapolated deformation.

is strengthened. The lower the outer drop viscosity, the lower the deformation, which is in agreement with Taylor [62] and Li *et al.* [79]. But as previously shown in Fig. 5.4, the lift force profile is at its maximum when the viscosities are equal across the phases.

Magnus Force and Saffman Lift Force

The Magnus lift force that acts upon a small spherical particle of diameter a with angular velocity $\vec{\Omega}$ in a fluid of density ρ_f is given by [78]

$$F_{\text{Magnus}} = \frac{1}{8}\pi a^3 \rho_f (\vec{u}_f - \vec{u}_p) \times \vec{\Omega} \quad (5.2)$$

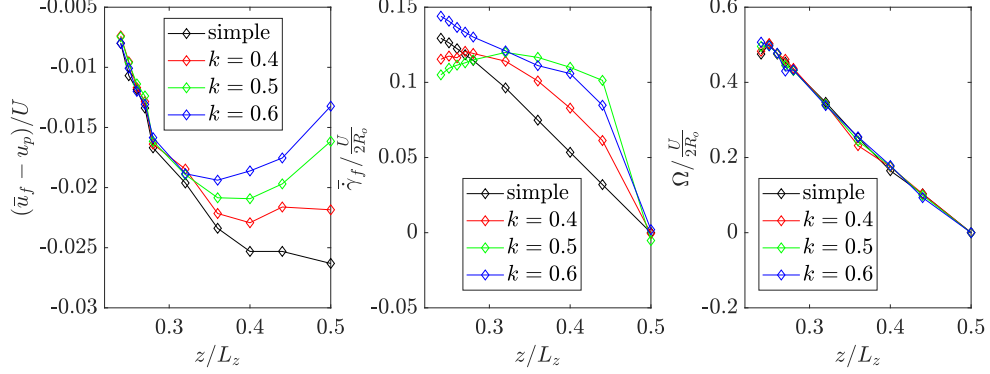


Figure 5.8. : The nondimensional slip velocity, effective shear rate, and rotation rate of the simple and compound drops.

where \vec{u}_f is the fluid velocity and \vec{u}_p is the particle velocity. To apply this functional form to the flow at hand, we first take that $a = 2R_o$, and find \vec{u}_f by taking a flow-direction projection average of the background fluid. The projection average is taken over the flow-direction projected area of the compound drop. This is done to closely approximate the centerline streamline velocity of the compound drop, which does not have an infinitesimal size. The particle velocity \vec{u}_p is taken as the volume average of the velocity inside the compound drop. Finally, $\vec{\Omega}$ is taken as the volume average of the vorticity inside the compound drop.

The Saffman lift force for a simple shear flow is given by

$$F_{\text{Saffman}} = 6.46a^2 \sqrt{\rho G \mu} (u_f - u_p) \quad (5.3)$$

where G is the local shear rate [53, 80]. To apply this functional form to the flow at hand, G is taken as the flow-direction projection average of du/dz . Upon applying the aforementioned steps to the flows at hand, we obtain the non-dimensional slip velocity $(u_f - u_p)/U$, the nondimensional effective shear rate $\frac{du}{dz} \frac{U}{2R_o}$, and nondimensional rotation rate $\Omega \frac{U}{2R_o}$ as shown in Fig. 5.8. Using those values, we can also compute the Magnus lift force and Saffman lift force as shown in nondimensional form in Fig. 5.9.

The lift profiles are not in a good agreement with Fig. 5.3. This is not too surprising since the functional forms of the Magnus force and Saffman force used are derived for

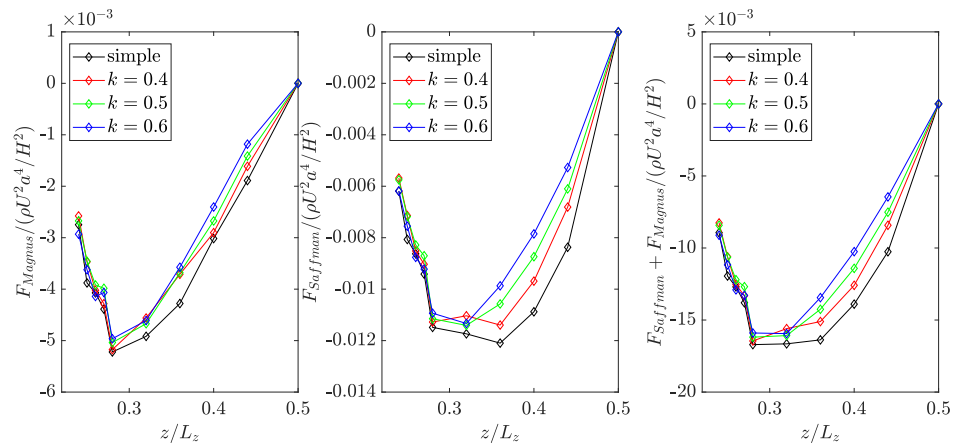


Figure 5.9. : Magnus force and Saffman lift force, calculated based on Fig. 5.8

a point spherical particle, and also because the Saffman force result assumes a simple shear gradient. Instead, we focus on the differences that arise between a simple drop and compound drops.

The difference in the lift force between a simple drop and a compound drop, as shown in Fig. 5.10, shows a qualitatively matching trend between the actually measured values and those computed from the Magnus and Saffman forces. However, the contributions to the difference in lift force arising from Magnus and Saffman forces are increased by 25 times in Fig. 5.10. The constant 25 is arbitrarily chosen so that the difference in the lift forces between the two methods match in the near-centerline region of the channel. Since the functional forms for the Magnus and Saffman forces are derived for a point spherical particle, we are more interested in finding a qualitative functional relationship that explains where the lift force difference between simple and compound drop arises, rather than the exact quantitative form. Furthermore, since we do not consider the wall-induced lift force, which dominates in the near-wall region, comparing the lift force from the different approaches near the wall does not make sense. From these comparisons, while we cannot conclusively determine the coefficient at play that determines the lift force, we can see that the drop slip velocity, effective shear rate, and drop rotation rate play important roles in differentiating the lift force profiles of compound drops from that of a simple drop.

Limitation of the Current Lift Force Model

While this method of predicting the lift force difference works well in the inner region of the channel, we see that the near-wall region scaling is not as good. As previously mentioned, this is not surprising since we did not account for the wall-induced lift force.

Another limitation of this scaling method is that it does not predict the lift force difference well when the outer drop (or simple drop) viscosity changes. Namely, we've previously shown that the lift force of compound drops in the inner region (*i.e.* away

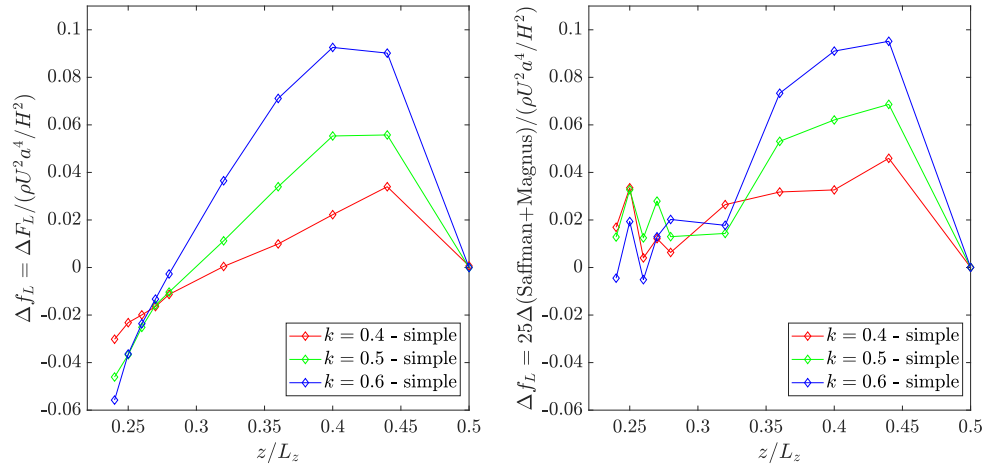


Figure 5.10. : Lift force difference between simple drop and compound drops. The simple drop lift force is taken as baseline and the difference to compound drop lift is shown, based on (left): the measurement (Fig. 5.3) and (right): The Magnus and Saffman forces combined (Fig. 5.9.)

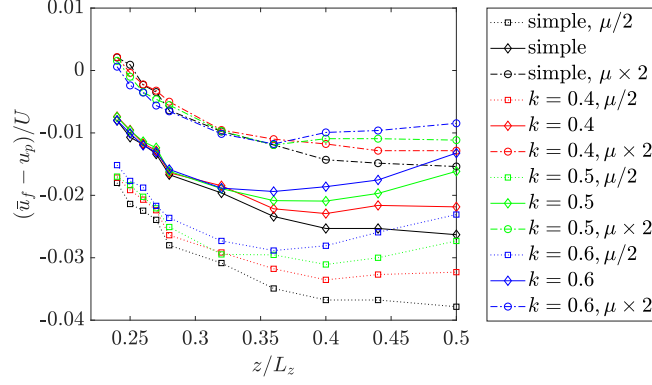


Figure 5.11. : The non-dimensional slip velocity over simple and compound drops with varying radii ratio and varying viscosities. The viscosities of simple drop or outer drop are varied as $\mu_{\text{new}}/\mu_{\text{old}} = [1/2, 1, 2]$.

from near-wall region) is less if the viscosity of the outer drop is either decreased or increased. This is not the trend that the Magnus and Saffman force calculations predict. The calculations instead predict that the lift force of equal viscosity system to lie between the lower and higher viscosity cases. This prediction is greatly influenced by the slip velocity changes with varying viscosities, as shown in Fig. 5.11.

We see that there is a monotonic relation between the viscosity of the outer drop (or simple drop) with the slip velocity. Since both Magnus force and Saffman force vary linearly with the slip velocity, their calculations yield results that do not agree well with what is found through the PI controller. There exists additional scaling with viscosity change that is currently unknown.

6. SUMMARY

We numerically investigated the temporal evolution of eccentric compound droplets subject to a simple shear flow with equal viscosities and densities in all phases. When the eccentricity is confined within the plane of shear, a “revolving” motion is observed for the inner droplet. Throughout the revolving motion, the inner droplet orbits about and slowly migrates away from the center of the outer droplet until only a thin film of liquid remains between the inner and outer interfaces, at which point the inner droplet revolves about the periphery of the outer interface in a limit cycle behavior. When the eccentricity is normal to the plane of shear, a “drifting” motion is observed, where the inner drop moves perpendicularly to the plane of shear, slowly increasing the eccentricity. The time scale relevant to the drifting motion is similar to that of the outward motion in the revolving motion.

Revolving and drifting motions increase the eccentricity of the compound droplet when $Re \leq 5$, $Ca_o \leq 0.1$ and $Ca_i < 0.1$, and are not affected by k in the range 0.4-0.6. Because simple shear flows are ubiquitous and easy to reproduce, and because they form the basis of linearized analysis of more complicated flows, this research sheds a new light into understanding the temporal evolution and eccentric breakup mechanism of compound droplets.

We also numerically investigated the temporal dynamics of concentric compound drop migration into several equilibrium configurations within a pressure-driven rectangular channel with $Re = O(1)$ and $Ca = O(0.1)$. Three equilibria - centerlined, pair vortex (inner), and pair vortex (outer) - are sensitive to initial placement, whereas the single vortex equilibrium is preferred given a general initial placement without explicit symmetry about the channel. In all equilibria except the centerlined equilibrium, the streamlines inside the outer drop encircle the inner drop. The placement or the size of

the inner drop in the either pair vortex equilibrium has little effect on the equilibrium position or deformation of the outer drop.

When the compound drop is too large compared to the channel, or when the aspect ratio of the channel is uniform, single vortex equilibrium disappears and pair vortex (outer) is preferred. Additionally, given a large enough compound drop relative to the rectangular channel, the wall effect dictates that the placement of the outer drop is centered in the channel while the inner drop can be placed eccentrically.

While there were some differences in the compound drop placements when the radii ratio was changed, the difference was small. To better aid in sorting of compound drops depending on the radii ratio, we looked at the lift force profile at various positions along the channel. The lift force profile showed a distinct difference between a compound drop and a simple drop, and also among compound drops with different radii ratio. This difference was much larger than the difference that results from changing the viscosity of the outer drop, which suggests a large application window. Further, we discussed the possible origin of the lift force difference between compound drop and simple drop, and showed that the functional forms of Magnus force and Saffman force give a good qualitative agreement, but also showed that there is an additional scaling due to viscosity change that is not yet understood.

Being able to predict the migration dynamics and the final configurations of compound drops in a pressure-driven channel has many different immediate applications such as in flow-focusing devices, sorting of compound drops, and in creating compound drops with predetermined geometry. Additionally, understanding the flow field inside the compound drop at the equilibrium configurations is important in extending the knowledge in predicting the dynamics of compound drops with multiple inner drops, or in predicting possible equilibria of triple - or higher - emulsions.

REFERENCES

REFERENCES

- [1] K. J. Lissant. Emulsion and emulsion technology, vol, i. *M Dekker, New York*, page 34, 1974.
- [2] Joseph Antoine Ferdinand Plateau. *Experimental and theoretical researches on the figures of equilibrium of a liquid mass withdrawn from the action of gravity, etc.* Smithsonian Institution, 1863.
- [3] Lord Rayleigh. On the capillary phenomena of jets. In *Proc. R. Soc. London*, volume 29, pages 71–97, 1879.
- [4] A. Sauret and H. C. Shum. Forced generation of simple and double emulsions in all-aqueous systems. *Appl. Phys. Lett.*, 100(15):154106, 2012.
- [5] M. L. Fabiilli, J. A. Lee, O. D. Kripfgans, P. L. Carson, and J. B. Fowlkes. Delivery of water-soluble drugs using acoustically triggered perfluorocarbon double emulsions. *Pharm. Res.*, 27(12):2753–2765, Dec 2010.
- [6] D. Lee and D. A. Weitz. Double emulsion-templated nanoparticle colloidosomes with selective permeability. *Adv. Mater.*, 20(18):3498–3503, 2008.
- [7] A. S. Utada, E. Lorenceau, D. R. Link, P. D. Kaplan, H. A. Stone, and D. A. Weitz. Monodisperse double emulsions generated from a microcapillary device. *Science*, 308(5721):537–541, 2005.
- [8] M. Abkarian, M. Faivre, and A. Viallat. Swinging of red blood cells under shear flow. *Phys. Rev. Lett.*, 98:188302, Apr 2007.
- [9] H. C. Shum, D. Lee, I. Yoon, T Kodger, and D. A. Weitz. Double emulsion templated monodisperse phospholipid vesicles. *Langmuir*, 24(15):7651–7653, 2008. PMID: 18613709.
- [10] M. Fingas, B. Fieldhouse, and Z. D. Wang. The long term weathering of water-in-oil emulsions. *Spill Sci. Technol. Bull.*, 8(2):137–143, 2003. Longer-Term Weathering Processes of Spilled Oil.
- [11] Fernando Leal-Calderon, Jérôme Bibette, and Véronique Schmitt. *Double Emulsions*, pages 173–199. Springer New York, New York, NY, 2007.
- [12] R. E. Johnson and S. S. Sadhal. Fluid mechanics of compound multiphase drops and bubbles. *Annual Review of Fluid Mechanics*, 17(1):289–320, 1985.
- [13] H.-C. Kan, H. S. Udaykumar, W. Shyy, and R. Tran-Son-Tay. Hydrodynamics of a compound drop with application to leukocyte modeling. *Phys. Fluids*, 10(4):760–774, 1998.

- [14] C. Goubault, K. Pays, D. Olea, P. Gorria, J. Bibette, V. Schmitt, and F. Leal-Calderon. Shear rupturing of complex fluids: Application to the preparation of quasi-monodisperse water-in-oil-in-water double emulsions. *Langmuir*, 17(17):5184–5188, 2001.
- [15] S. Okushima, T. Nisisako, T. Torii, and T. Higuchi. Controlled production of monodisperse double emulsions by two-step droplet breakup in microfluidic devices. *Langmuir*, 20(23):9905–9908, 2004. PMID: 15518471.
- [16] I. G. Loscertales, A. Barrero, I. Guerrero, R. Cortijo, M. Marquez, and A. M. Gañán-Calvo. Micro/nano encapsulation via electrified coaxial liquid jets. *Science*, 295(5560):1695–1698, 2002.
- [17] R. Chambers and M. J. Kopac. The coalescence of living cells with oil drops. i. arbutia eggs immersed in sea water. *J. Cell. Comp. Physiol.*, 9(3):331–343, 1937.
- [18] M. J. Kopac and R. Chambers. The coalescence of living cells with oil drops. ii. arbutia eggs immersed in acid or alkaline calcium solutions. *J. Cell. Comp. Physiol.*, 9(3):345–361, 1937.
- [19] S. Torza and S.G. Mason. Three-phase interactions in shear and electrical fields. *J. Colloid Interface Sci.*, 33(1):67–83, 1970.
- [20] H. Lamb. *Hydrodynamics*, pages 594–599. Dover publications, New York, 1945.
- [21] G. I. Taylor. The viscosity of a fluid containing small drops of another fluid. *Proc. R. Soc. A*, 138(834):41–48, 1932.
- [22] R. G. Cox. The deformation of a drop in a general time-dependent fluid flow. *J. Fluid Mech.*, 37(3):601–623, 07 1969.
- [23] H. A. Stone and L. G. Leal. Breakup of concentric double emulsion droplets in linear flows. *J. Fluid Mech.*, 211:123–156, 02 1990.
- [24] X. Qu and Y. Wang. Dynamics of concentric and eccentric compound droplets suspended in extensional flows. *Phys. Fluids*, 24(12), 2012.
- [25] S. S. Sadhal and H. N. Oguz. Stokes flow past compound multiphase drops: the case of completely engulfed drops/bubbles. *J. Fluid Mech.*, 160:511–529, 11 1985.
- [26] Y. Song, J. Xu, and Y. Yang. Stokes flow past a compound drop in a circular tube. *Phys. Fluids*, 22(7), 2010.
- [27] S. Mandal, U. Ghosh, and S. Chakraborty. Effect of surfactant on motion and deformation of compound droplets in arbitrary unbounded stokes flows. *J. Fluid Mech.*, 803:200–249, 009 2016.
- [28] H. Haj-Hariri, A. Nadim, and A. Borhan. Reciprocal theorem for concentric compound drops in arbitrary stokes flows. *J. Fluid Mech.*, 252:265–277, 007 1993.
- [29] J. M. Rallison. The deformation of small viscous drops and bubbles in shear flows. *Annu. R. Fluid Mech.*, 16(1):45–66, 1984.
- [30] P. C.-H. Chan and L. G. Leal. The motion of a deformable drop in a second-order fluid. *J. Fluid Mech.*, 92(1):131–170, 05 1979.

- [31] M. Shapira and S. Haber. Low Reynolds number motion of a droplet in shear flow including wall effects. *Int. J. Multiphase Flow*, 16(2):305–321, 1990.
- [32] H. A. Stone. Fluid mechanics of compound multiphase drops and bubbles. *Annual Review of Fluid Mechanics*, 17(1):289–320, 1985.
- [33] G. Hetsroni and S. Haber. The flow in and around a droplet or bubble submerged in an unbound arbitrary velocity field. *Rheol. Acta*, 9(4):488–496, Nov 1970.
- [34] G. Segré and A. Silberberg. Behaviour of macroscopic rigid spheres in poiseuille flow part 1. Determination of local concentration by statistical analysis of particle passages through crossed light beams. *J. Fluid Mech.*, 14(1):115–135, 1962.
- [35] G. Segré and A. Silberberg. Behaviour of macroscopic rigid spheres in poiseuille flow part 2. experimental results and interpretation. *J. Fluid Mech.*, 14(1):136–157, 1962.
- [36] B. Chun and A. J. C. Ladd. Inertial migration of neutrally buoyant particles in a square duct: An investigation of multiple equilibrium positions. *Phys. Fluids*, 18(3):031704, 2006.
- [37] Y. W. Kim and J. Y. Yoo. The lateral migration of neutrally-buoyant spheres transported through square microchannels. *J. Micromech. Microeng.*, 18(6):065015, 2008.
- [38] A. A. S. Bhagat, S. S. Kuntaegowdanahalli, and I. Papautsky. Inertial microfluidics for continuous particle filtration and extraction. *Microfluid Nanofluidics*, 7(2):217–226, Aug 2009.
- [39] A. T. Ciftlik, M. Etti, and M. A. M. Gijs. High throughput-per-footprint inertial focusing. *Small*, 9(16):2764–2773, 2013.
- [40] A. Karnis, H. L. Goldsmith, and S. G. Mason. Axial migration of particles in poiseuille flow. *Nature*, 200:159–160, 1963.
- [41] A. Karnis and S. G. Mason. Particle motions in sheared suspensions. *J. Colloid Interface Sci.*, 24(2):164–169, 1967.
- [42] H. L. Goldsmith and S. G. Mason. The flow of suspensions through tubes. i. single spheres, rods, and discs. *J. Colloid Sci.*, 17(5):448–476, 1962.
- [43] X. Chen, C. Xue, L. Zhang, G. Hu, X. Jiang, and J. Sun. Inertial migration of deformable droplets in a microchannel. *Phys. Fluids*, 26(11):112003, 2014.
- [44] K. S. Chang and W. L. Olbricht. Experimental studies of the deformation and breakup of a synthetic capsule in steady and unsteady simple shear flow. *J. Fluid Mech.*, 250:609–633, 05 1993.
- [45] M. T. Sullivan and H. A. Stone. The role of feedback in microfluidic flow-focusing devices. *Phil. Trans. R. Soc. A*, 366(1873):2131–2143, 2008.
- [46] J. K. Klahn, J. J. M. Janssen, G. E. J. Vaessen, R. de Swart, and W. G. M. Agterof. On the escape process during phase inversion of an emulsion. *Colloids Surf., A*, 210(2–3):167 – 181, 2002.

- [47] Y. Chen, X. Liu, and M. Shi. Hydrodynamics of double emulsion droplet in shear flow. *Appl. Phys. Lett.*, 102(5):051609, 2013.
- [48] Y. Chen, X. Liu, and Y. Zhao. Deformation dynamics of double emulsion droplet under shear. *Appl. Phys. Lett.*, 106(14):141601, 2015.
- [49] Y. Chen, X. Liu, C. Zhang, and Y. Zhao. Enhancing and suppressing effects of an inner droplet on deformation of a double emulsion droplet under shear. *Lab Chip*, 15:1255–1261, 2015.
- [50] H. Hua, J. Shin, and J. Kim. Dynamics of a compound droplet in shear flow. *Int. J. Heat Fluid Flow*, 50:63–71, 2014.
- [51] S. Patlazhan, S. Vagner, and I. Kravchenko. Steady-state deformation behavior of confined composite droplets under shear flow. *Phys. Rev. E*, 91:063002, Jun 2015.
- [52] K. A. Smith, J. M. Ottino, and M. Olvera de la Cruz. Encapsulated drop breakup in shear flow. *Phys. Rev. Lett.*, 93:204501, Nov 2004.
- [53] P. G. Saffman. The lift on a small sphere in a slow shear flow. *J. Fluid Mech.*, 22(2):385–400, 06 1965.
- [54] B. P. Ho and L. G. Leal. Inertial migration of rigid spheres in two-dimensional unidirectional flows. *J. Fluid Mech.*, 65(2):365–400, 1974.
- [55] J.-P. Matas, J. F. Morris, and É Guazzelli. Inertial migration of rigid spherical particles in poiseuille flow. *J. Fluid Mech.*, 515:171–195, 2004.
- [56] X. Shao, Z. Yu, and B. Sun. Inertial migration of spherical particles in circular poiseuille flow at moderately high reynolds numbers. *Phys. Fluids*, 20(10):103307, 2008.
- [57] Amir Hossein Raffee, Sadegh Dabiri, and Arezoo M. Ardekani. Elasto-inertial migration of deformable capsules in a microchannel. *Biomicrofluidics*, 11(6), 2017.
- [58] C. Zhou, P. Yue, and J. J. Feng. Deformation of a compound drop through a contraction in a pressure-driven pipe flow. *Int. J. Multiphase Flow*, 34(1):102–109, 2008.
- [59] J. Wang, X. Li, X. Wang, and J. Guan. Possible oriented transition of multiple-emulsion globules with asymmetric internal structures in a microfluidic constriction. *Phys. Rev. E*, 89:052302, May 2014.
- [60] S. Dabiri, J. Lu, and G. Tryggvason. Transition between regimes of a vertical channel bubbly upflow due to bubble deformability. *Phys. Fluids*, 25(10), 2013.
- [61] B. Bunner and G. Tryggvason. Effect of bubble deformation on the properties of bubbly flows. *J. Fluid Mech.*, 495:77–118, 11 2003.
- [62] G. I. Taylor. The formation of emulsions in definable fields of flow. *Proc. R. Soc. A*, 146(858):501–523, 1934.

- [63] T. Hayase, J. A. C. Humphrey, and R. Greif. A consistently formulated QUICK scheme for fast and stable convergence using finite-volume iterative calculation procedures. *J. Comput. Phys.*, 98(1):108–118, 1992.
- [64] A. J. Chorin. Numerical solution of the Navier-Stokes equations. *Math. Comp.*, 22:745–762, 1968.
- [65] R. D. Falgout and U. M. Yang. *hypre: A Library of High Performance Pre-conditioners*, pages 632–641. Springer Berlin Heidelberg, Berlin, Heidelberg, 2002.
- [66] S. O. Unverdi and G. Tryggvason. A front-tracking method for viscous, incompressible, multi-fluid flows. *J. Comput. Phys.*, 100(1):25–37, 1992.
- [67] J. W. Ha, Yosang Yoon, and L. G. Leal. The effect of compatibilizer on the coalescence of two drops in flow. *Physics of Fluids*, 15(4):849–867, 2003.
- [68] F.D. Rumscheidt and S.G. Mason. Particle motions in sheared suspensions xii. deformation and burst of fluid drops in shear and hyperbolic flow. *J. of Colloid Sci.*, 16(3):238–261, 1961.
- [69] S. K. Veerapaneni, Y.-N. Young, P. M. Vlahovska, and J. Bławdziewicz. Dynamics of a compound vesicle in shear flow. *Phys. Rev. Lett.*, 106:158103, Apr 2011.
- [70] Z. Che, Y. F. Yap, and T. Wang. Flow structure of compound droplets moving in microchannels. *Phys. Fluids*, 30(1):012114, 2018.
- [71] S. Mortazavi and G. Tryggvason. A numerical study of the motion of drops in poiseuille flow. part 1. lateral migration of one drop. *J. Fluid Mech.*, 411:325–350, 2000.
- [72] S Kim and S Dabiri. Transient dynamics of eccentric double emulsion droplets in a simple shear flow. *Phys. Rev. Fluids*, 2:104305, Oct 2017.
- [73] Y.-C. Tan, Y. L. Ho, and A. P. Lee. Microfluidic sorting of droplets by size. *Microfluid Nanofluidics*, 4(4):343, Jun 2007.
- [74] S Kim and S Dabiri. Lateral migration of compound drops in low reynolds number poiseuille flow. *Phys. Rev. Fluids (submitted)*.
- [75] C. Schaaf and H. Stark. Inertial migration and axial control of deformable capsules. *Soft Matter*, 13:3544–3555, 2017.
- [76] E. S. Asmolov. The inertial lift on a spherical particle in a plane poiseuille flow at large channel reynolds number. *J. Fluid Mech.*, 381:63–87, 1999.
- [77] D. Di Carlo, J. F. Edd, K. J. Humphry, H. A. Stone, and M. Toner. Particle segregation and dynamics in confined flows. *Phys. Rev. Lett.*, 102:094503, Mar 2009.
- [78] J. Zhang, S. Yan, D. Yuan, G. Alici, N.-T. Nguyen, M. E. Warkiani, and W. Li. Fundamentals and applications of inertial microfluidics: a review. *Lab Chip*, 16:10–34, 2016.

- [79] J. Li, Y. Y. Renardy, and M. Renardy. Numerical simulation of breakup of a viscous drop in simple shear flow through a volume-of-fluid method. *Phys. Fluids*, 12(2):269–282, 2000.
- [80] H. A. Stone. Philip saffman and viscous flow theory. *J. Fluid Mech.*, 409:165–183, 2000.

VITA

VITA

Research Interest

I am interested in multiphase flows of Newtonian fluids. In particular, I am interested in the computational study of simple drop, compound drop, and bubble dynamics in low Reynolds number flows.

Education

- **Ph.D.** in Mechanical Engineering - Purdue University, December 2019
 Recipient of Kohr Graduate Fellowship
 Recipient of Lambert Graduate Teaching Fellowship
 Recipient of Magoon Award for Excellence in Teaching
- **M. Eng.** in Mechanical & Aerospace Engineering - Cornell University, August 2013
- **B.S.** in Mechanical Engineering - California Institute of Technology, June 2012
- **B.S.** in Physics - California Institute of Technology, June 2012

Publications

- S. Kim and S. Dabiri, “Cross stream lift force on a compound drop in 3D rectangular Poiseuille Flow,” *Physical Review Fluids*, in preparation.
- S. Kim and S. Dabiri, “Lateral migration of single compound drop in low Reynolds number Poiseuille flow,” *Physical Review Fluids*, submitted.
- M. Ganesh, S. Kim, and S. Dabiri, “Induced mixing in stratified fluids by rising bubbles in a thin gap,” *Physical Review Fluids*, submitted.

- S. Kim and S. Dabiri, “Transient dynamics of eccentric double emulsion droplets in a simple shear flow,” *Physical Review Fluids*, **2**, 104305 (2017)
- S. Kim and S. Dabiri, “Dynamics of double emulsion droplets in shear and channel flows,” *9th International Conference on Multiphase Flow (ICMF 2016)*, May22-27, 2016, Florence, Italy.
- M. Bryant, J. Fitzgerald, S. Miller, J. Saltzman, S. Kim, Y. Lin, and E. Garcia, “Climbing robot actuated by meso-hydraulic artificial muscles”, *Proc. SPIE 9057*, Active and Passive Smart Structures and Integrated Systems 2014, March 9, 2014, San Diego, California, USA.

Conference Presentations/Contributions

- M. Ganesh, S. Kim, and S. Dabiri, “Induced mixing in stratified fluids by rising bubbles in a thin gap,” *72nd Annual Meeting of the APS Division of Fluid Dynamics (APS DFD 2019)*, Nov 23-26, 2019, Seattle, WA, USA
- S. Dabiri and S. Kim, “Migration and Equilibrium Configuration of Double Emulsion Drops in Microfluidic Channels,” *2018 AIChE Annual Meeting*, Oct 28 - Nov 2, 2018, Pittsburgh, PA, USA
- S. Kim and S. Dabiri, “Lateral migration and Equilibrium of Compound Drops in Low Reynolds Number Poiseuille Flow,” *70th Annual Meeting of the APS Division of Fluid Dynamics (APS DFD 2017)*, Nov 19-21, 2017, Denver, CO, USA
- S. Kim and S. Dabiri, “Effect of eccentricity in compound droplets subject to a simple shear flow,” *69th Annual Meeting of the APS Division of Fluid Dynamics (APS DFD 2016)*, Nov 20-22, 2016, Portland, OR, USA.

Teaching Experience

- Undergraduate Lead Instructor, Fall 2019
Currently teaching a 31-student section of senior level undergraduate course, ABE450: Design and Optimization in Finite Element Analysis. Responsible for preparing and providing feedback on lectures, homeworks, ANSYS projects, and exams.
- Undergraduate Co-Instructor: Lambert Graduate Teaching Fellowship, Fall 2018
Taught a 64-student section out of a 302-student junior-to-senior level undergraduate course, ME309: Fluid Mechanics. Covered 40 lectures, held office hours, and helped write and proctor exams.
- Graduate Teaching Assistant - Spring 2016, Spring 2017, Fall 2017, Spring 2018
Lead lab sections by introducing the concepts and the experiments, prepared quizzes with other teaching assistants, and provided feedback on the lab reports and quizzes.
- Women in Engineering Program Outreach - Summer 2016, Summer 2017
Demonstrated and explained fluid mechanics phenomena to middle school female students with the goal of attracting them to the STEM fields.